Chapter 2
Coupled-Core Fluxgate Magnetometer

Magnetic sensors are inherently nonlinear systems, which have been been used over many years to detect weak magnetic signals for a wide variety of applications. For instance: biomedical tracking of magnetic particles, e.g., MRI machines commonly used for diagnosing multiple sclerosis, brain tumors, and spinal infections; geological equipment, e.g., NASA explorers; homeland defense, e.g., detection of mines and explosives. Using ideas and methods from nonlinear dynamics research in Engineering, Mathematics, and Physics, we show that higher sensitivity, lower power consumption, and reduced costs, can all be achieved through an integrating approach that combines a new sensing technique, the *Residence Time Detection (RTD)*, with a novel *Network Sensor Architecture*, where the power of multiple sensors is integrated into a single system, see Fig. 2.1.

We demonstrate [168, 261, 262] that under the proposed approach, fluxgates magnetometers, in particular, can become very competitive against the most sensitive of all sensors, the SQUID (Superconducting Quantum Interference Devices), at a fraction of the cost and size of SQUIDs. The ideas are model-independent, so they can be used to enhance the performance of many other type of sensors such as electric field sensors and gyroscopes.

2.1 Fluxgate Technology

Early development of fluxgate magnetometers started around World War II, when fluxgate sensors were used by airborne magnetic surveys and for the detection of submarines. They were further developed for geomagnetic studies and mineral prospecting, and later for work on the Moon [105], for magnetic measurement in outer space [290, 344, 365], and for many other applications [158, 169, 312] as well. Readers interested in the advances of fluxgates are referred to the article in [151].

V. In and A. Palacios, *Symmetry in Complex Network Systems*,
Understanding Complex Systems, DOI 10.1007/978-3-662-55545-3_2

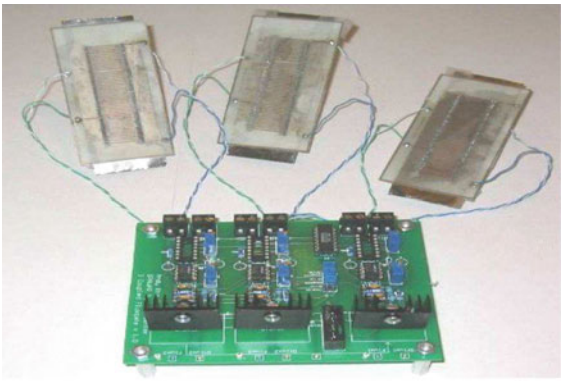

Fig. 2.1 First generation of a coupled fluxgate magnetometer. The network-based sensor is about 400 times more sensitive than any individual counter part

Classical fluxgate sensors consist of two identical ferromagnetic cores that are deeply driven into saturation [293]. This is based on what is referred to as the magnetic saturation circuit. The two parallel bars of a ferromagnetic material (which establishes the axis direction) are placed closely together. Each bar is wound with a primary coil, but the direction in which the coil is wrapped around the bars is reversed, see Fig. 2.2.

Two periodic counter-phased magnetic fluxes are induced through the excitation currents I_e, driving the magnetic cores periodically into saturation in opposite senses: the pulsed signals $V_i(t)$, $(i = 1, 2)$, given by each pick up coil, oscillate back and forth at the forcing frequency. The time waveforms of these signals are shown in Fig. 2.2b,c respectively. For a symmetric core magnetization and in the absence of the target signal, the output voltage signal, denoted by $V_o(t) = V_1(t) - V_2(t)$, is zero. An external (assumed to be dc or extremely low frequency) magnetic field H_x leads to an asymmetry in the cores magnetization and, hence, produces a non-zero output voltage $V_o(t)$ (see the bottom of Fig. 2.2c).

As we discussed in Chap. 1, to detect a small target signal (dc or low-frequency), typically the *standard* readout mechanism is employed. Recall that in this readout mechanism the absence of a target signal yield only odd harmonics in the power spectral density of the output signal. Even harmonics only appear under the presence of a target signal. Then the response at the second even harmonic is used to detect and quantify the external target signal, see Fig. 1.6.

Magnetic materials such as iron, cobalt, and steel, contain tiny subatomic regions of magnetism called domains. When these domains align the result is a magnetic field. Now in any ferrous object the magnetic lines of force or flux are greatest at the ends of a magnet or dipole. Of course, magnetic forces vary according to size, shape, and orientation of the object. Consider a simple rifle. This rifle can be approximated by a magnetic dipole and has its own variations of magnetic lines of force. These lines of force influence the Earth's magnet forces which cause a change in the Earth's ambient local magnetic field near the rifle. This change is commonly know as an anomaly. Fluxgate magnetometers can measure this magnetic field anomalies. The amount of measurable change in an anomaly force depends on the size and distance from the

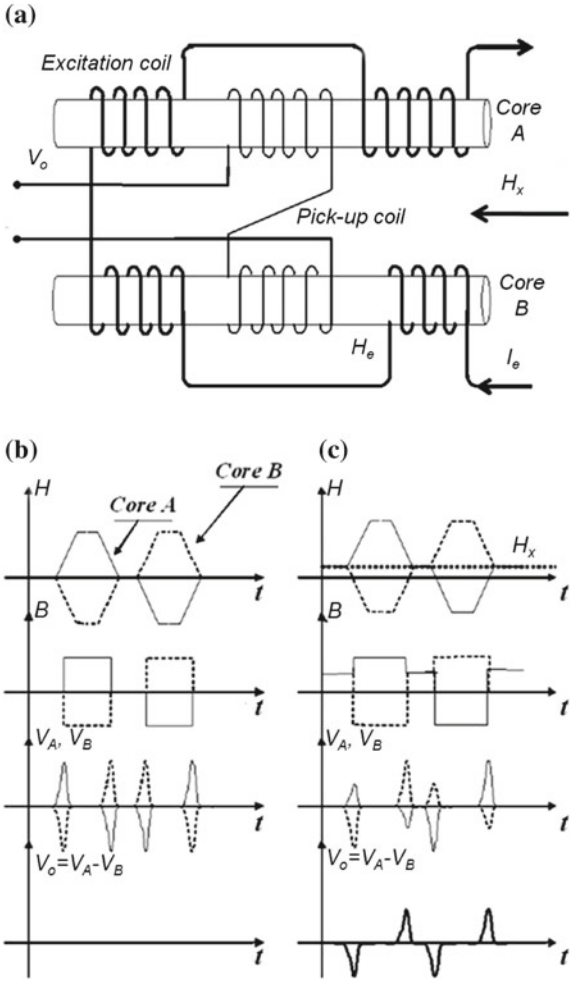

Fig. 2.2 **a** Arrangement for a traditional fluxgate magnetometer as proposed by Forster [124] **b** signals in time domain with zero external target magnetic field (output is zero) and **c** in the presence of a non zero target magnetic field. In particular, the magnetizing field, the corresponding magnetic flux, the voltages induced at the pick-up coils, and the resulting output voltage $V_o(t)$ are shown in the absence **(b)** and in the presence **(c)** of the target magnetic field H_x

device. A basic idea of some of the typical measurements can be seen in Table 2.1, which was originally produced by S. Breiner [52]. Today's highly specialized fluxgate devices boast laboratory sensitivity levels as low as $10pT/\sqrt{Hz}$.

Although fluxgates were thought to have reached their fundamental limits of sensitivity [223], new research and development have recently sparked a renewed interest in using fluxgate sensors as an inexpensive alternative for certain applications [335, 336, 339]. In the biomedical field, for instance, research with magnetic tracers has lead scientists to consider using fluxgate sensors to study the mechanical activity of the large intestine [120]. Other potential applications include remote sensing [158], geological explorations of the deep ocean [169], vehicle guidance in agriculture [34], and traffic control [216]. Magnetic disturbances can be used to classify vehicles for toll road applications. A sensors is placed in the lane of traffic provides a signal output

Table 2.1 Magnetic fields measurements for different objects vary according to distance and size of each individual object. Units appear in nano-Tesla nT

Ferrous Components	"Near"	"Far"
Ship (100 tons)	100 ft (300-700 nT)	1000 ft (0.3-0.7 nT)
Train Engine	500 ft (5-200 nT)	1000 ft (1-50 nT)
Automobile (1 ton)	30 Feet (40 nT)	100 ft (1 nT)
Rifle	5 ft (10-50 nT)	10 ft (2-10 nT)
Screwdriver (5")	5 ft (5-10 nT)	10 ft (0.5-1 nT)

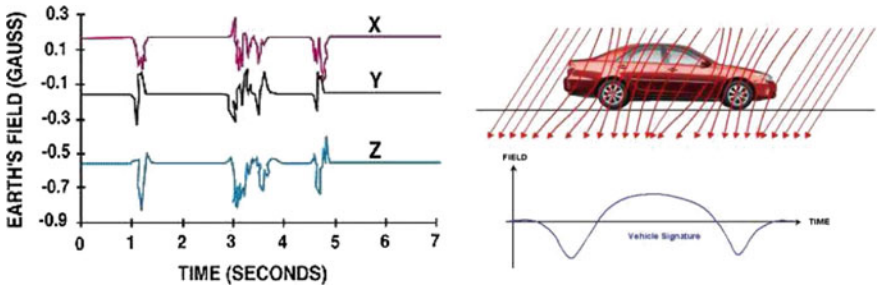

(a) Car in Field (b) Vehicle Detection

Fig. 2.3 Fluxgate sensors can detect Earth field anomalies as three cars drive by. *Left* Sensors provide the X, Y, and Z axes and show unique signatures for the three different types of vehicles. *Right* Vehicle identification can be carried out using pattern recognition algorithms

for vehicles passing over it. Figure 2.3 shows a magnetometer output for three vehicles driving over it for roughly 1, 3, and 5 s. The type of vehicle (e.g., car, truck, bus) can be classified through pattern recognition and matching algorithms. A two-axes fluxgate magnetometer detects changes in the vertical and horizontal components of the Earth's magnetic field produced by a ferrous metal vehicle. It detects stationary and moving vehicles.

Motivated by this renewed interest on fluxgate magnetometers, we started (around year 2002) to investigate the possibility of developing a novel approach for a low-cost, low-power, highly sensitive fluxgate magnetometer. The approach was innovative because it incorporated a network architecture, via coupled cell systems, with a novel readout mechanism based on symmetry-breaking effects on heteroclinic waveforms. Instead of using a traditional fluxgate with two cores, the work was carried out with a single-core. To develop a robust and programmable dc (ε constant) sensing device, we investigated the theoretical limit [218, 223] of magnetic-field sensitivity of a network of fluxgate sensors. Since the limit depends, mainly, on the ability of the network to produce stable self-biasing oscillations, we studied the behavior of a coupled fluxgate system in response to changes in parameters. In particular, the existence and stability of periodic solutions in response to changes in the coupling strength, the topology of connections, and the temperature-related parameters.

In this chapter we describe the overall endeavor, which lead to the design and, ultimately, to the fabrication of the most sensitive fluxgate-type of magnetometer on the planet. We start with Landau's theory [247] on the physics of *phase transitions*, which allows to formulate a mathematical model in the form of a continuous differential equation for the magnetization state of a fluxgate device.

2.2 Modeling Single-Core Dynamics

We consider a single-core fluxgate with a two-coil structure (a primary coil and a secondary coil) wound around a suitable magnetic core, as is depicted in Fig. 2.4. The magnetization of the core is governed by the excitation field H_e produced in the primary coil and the core is composed of a ferromagnetic material with the characteristic"sharp" input-output hysteresis loop, corresponding to a bistable potential energy function, which underpins the system dynamics; the minima of this potential energy function correspond to the two (stable) steady magnetization states, as it was originally described in Chap.1, see Fig. 1.5. In order to reverse the core magnetization, a suprathreshold excitation field is required. Here, the "threshold" represents the minimum field required to switch the saturation of the material. Mathematically, it corresponds to the inflection point(s) in the potential function. With an alternating excitation (or bias) magnetic field H_e, the output voltage V_o at the secondary coil will be alternating and symmetric in time. The presence of an external "target" magnetic field H_x will break this symmetry and the resulting temporal asymmetry can be used to monitor the target field amplitude.

A simple way to model the ferromagnetic dynamics is through an Ising-type model. We assume the core to be composed of a set of atomic magnets, called "spins", arranged on a regular lattice that represents the crystal structure of the core [51]. Thermal fluctuations tend to disrupt the orientation of the spins while spin interactions tend to align the spins with each other. When the temperature T exceeds a critical temperature T_c, called the Curie temperature, the system exhibits a *phase*

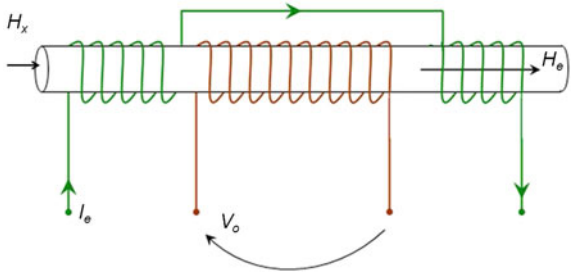

Fig. 2.4 Single core fluxgate sensor consist of two coils wound (in opposite directions) around a ferromagnetic core. Fluxgates show bistable dynamics with a hysteresis loop. Thus one coil is used to induce (via a biasing signal) the core to oscillate between two magnetization states ± 1. The other coil is used as a pick-up coil to detect the core response

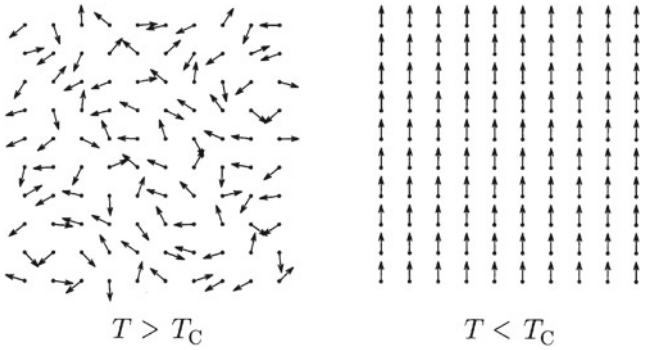

Fig. 2.5 *Left* A ferromagnet in a paramagnet state, well above the critical temperature T_c the magnetic spins are randomly organized. *Right* Below the critical temperature, a majority of the spins are uniformly organized in one of two states, "up" or "down". *Source Introduction to the Theory of Neural Computation* [170]

transition [38, 377] from a *paramagnet state* with little magnetization properties to a *ferromagnetic state*, where magnetization is uniform, see Fig. 2.5.

A particularly useful simplification is to consider spin 1/2 magnetic materials, so that only two distinct directions are possible: "spin up" ($S_i = +1$) and "spin down" ($S_i = -1$), where S_i is the state variable that describes the orientation of the spin found at lattice i. Then the average magnetic field $\langle h_i \rangle$ at spin S_i is determined by adding the average contributions from all neighboring spins S_j and from any external h^{ext} applied field through:

$$\langle h_i \rangle = \sum_{j \to i} w_{ij} \langle S_j \rangle + h^{ext}, \tag{2.1}$$

where w_{ij} is the coupling strength of the influence of spin S_j on S_i. The applied field h_i can induce the magnetic spin to switch back and forth between its two states $+1$ and -1. The actual switching mechanism can be modeled by an activation function:

$$\langle S_i \rangle = \tanh(\beta \langle h_i \rangle). \tag{2.2}$$

where the parameter β is related to the temperature T through $\beta = 1/(k_B T)$, with k_B being Boltzmann's constant. Substituting Eq. (2.1) into Eq. (2.2), shows that the *average magnetization* is given by

$$\langle S_i \rangle = \tanh(\beta \sum_{j \to i} w_{ij} \langle S_j \rangle + \beta h^{ext}). \tag{2.3}$$

Our interest is in the ferromagnetic state, in which $\langle S_i \rangle = \langle S \rangle$. Assuming identical coupling strengths $w_{ij} = 1/N$, where N is the number of spins, we find a single equation for the average magnetization:

$$\langle S\rangle = \tanh(\beta\langle S\rangle + \beta h^{ext}). \tag{2.4}$$

An extension of this last equation with continuous updating of the average magnetization state leads to the following simple model of the fluxgate core dynamics

$$\tau\frac{dx}{dt} = -x + \tanh\left(\frac{x+h}{T}\right), \tag{2.5}$$

where τ is a relaxation parameter, $x = \langle S\rangle$, $k_B = 1$ so that $\beta = 1/T$ is a pseudo-temperature parameter, and $h = h^{ext}$. There is a close analogy of this model with those of artificial Hopfield neural networks [179]. The saturation nonlinearity of the tanh function, for instance, is equivalent to the activation function that controls the response of individual neurons. There is also an analogy with the *energy function* introduced by Hopfield [179] in neural network theory. In our case,

$$\tau\frac{dx}{dt} = -\frac{\partial U}{\partial x}(x,t),$$

where $U(x,t) = \dfrac{x^2}{2} - T\ln\left(\cosh\left(\dfrac{x+h}{T}\right)\right)$. Although we have used various simplifying assumptions to arrive at the model equation (2.5), the theoretical work presented later shows good agreement with experimental measurements of the dynamics of the entire core.

Next we study in great detail the effects of coupling various fluxgate sensors.

2.3 Coupled Single-Domain System

We now consider a network of N fluxgate magnetometers coupled unidirectionally in a ring fashion, as is shown schematically in Fig. 2.6(left). For the time being, we assume the individual fluxgates to be identical as well as the common coupling strength λ. But later on we consider the effects of non-homogeneities. Thus the global symmetries of the network are described by the group $\mathbf{Z}_N$ of cyclic permutations of N objects.

The collective behavior of the network of fluxgate sensors of Fig. 2.6 is governed by the following system of Ordinary Differential Equations (ODE):

$$\tau_i\dot{x}_i = -x_i + \tanh(c(x_i + \lambda x_{i+1} + \varepsilon)), \tag{2.6}$$

where $x_i(t)$ represents the (suitably normalized) magnetic flux at the output (i.e. in the secondary coil) of each individual ith unit, with $i = 1,\ldots N \bmod N$, and $\varepsilon \ll U_0$ is an externally applied dc magnetic flux, c is a temperature-dependent nonlinearity parameter (each element is bistable for $c > 1$), and U_0 is the energy barrier height of any of the elements, absent the coupling. Notice that the (uni-directional) coupling

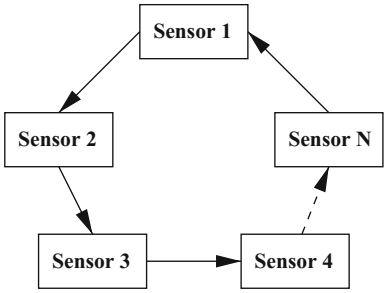

Fig. 2.6 *Left* Schematic of a network-based sensor architecture. Individual sensors are coupled unidirectionally in a ring fashion. The symmetries of the network are described by the group $\mathbf{Z}_N$ of cyclic permutations of N objects

term, having strength λ, which is assumed to be equal for all three elements, is *inside* the nonlinearity. This is a direct result of the mean-field nature of the description in the fluxgate magnetometer, the coupling is through the induction in the primary or "pick up" coil.

Geometric Description of Solution Set by Group Orbits. We start with a brief description of the solution sets for Eq. (2.6) as the coupling strength λ varies. The bifurcation methods generalize to arbitrary N, but the detailed specifics for finding and visualizing the basins of attraction are limited to 3D, so we focus on $N = 3$. When N is even heteroclinic connections do not exist [56, 195] nor periodic oscillations—only equilibrium solutions. Without loss of generality, the external field ε is set to zero and after re-scaling time the time constant can be set to $\tau_i = 1$. The specific system of equations used for our subsequent figures satisfies:

$$\begin{aligned} \dot{x_1} &= -x_1 + \tanh(c(x_1 + \lambda x_2)) \\ \dot{x_2} &= -x_2 + \tanh(c(x_2 + \lambda x_3)) \\ \dot{x_3} &= -x_3 + \tanh(c(x_3 + \lambda x_1)), \end{aligned} \tag{2.7}$$

where $c = 3$. Observe now that since the activation function tanh is odd, Eq. (2.7) remains unchanged under the transformation $x_i \mapsto \pm x_i$. Under unidirectional coupling with positive feedback the network equations are also unchanged under the cyclic transformation $x_i \mapsto x_{i+1}$. It follows that the symmetries of the coupled bistable system (2.7) are captured by the 24-elements group

$$\Gamma \simeq \mathbf{Z}_2^3 \otimes \mathbf{Z}_3,$$

which is generated by

$$\begin{aligned} (x_1, x_2, x_3) &\mapsto (\pm x_1, \pm x_2, \pm x_3) \\ (x_1, x_2, x_3) &\mapsto (x_2, x_3, x_1). \end{aligned}$$

The various type of solutions of Eq. (2.7) can be observed in the bifurcation diagram shown in Fig. 2.7, which was computed with the aid of the continuation software package AUTO [101]. When the coupling parameter is sufficiently large, and negative, then all solutions other than the unstable trivial solution and its 1D

symmetric stable manifold, emanating along the line $x_1 = x_2 = x_3$, are attracted to a stable asymmetric periodic orbit with 3-fold symmetry. The oscillations occur for $\lambda < \lambda_c$, where λ_c is a critical coupling strength to be determined later on. At the other end, when the coupling parameter is sufficiently large, and positive, or at least $\lambda > \lambda_c$, then all solutions other than the unstable trivial solution and its 2D stable manifold are attracted to one of two stable symmetric equilibria. The same result ensues if N is even, or if the coupling is bidirectional.

For values of λ slightly less than λ_c, there is a small interval $\lambda_{HB} \leq \lambda \leq \lambda_c$ where global oscillations and synchronous equilibria of the form $(x_1, \ldots, x_N) = (x*, \ldots, x*)$ can coexist. In this interval, complex transitions that involve multiple equilibrium points, periodic solutions, and heteroclinic connections are observed. A close-up view of the interval of bistability of large amplitude oscillations and stable synchronous equilibria is also included in Fig. 2.7. The four branches of unstable equilibria that appear via saddle-node bifurcations (labeled LP) correspond to non-synchronous equilibria.

To unravel those transitions we start with a large negative value of λ and replot the bifurcation diagram using x_1 in Fig. 2.8. As λ increases, there is a pitchfork bifurcation, producing two new symmetric equilibria moving away from the origin along its 1D stable manifold. As λ further increases, the 1D stable manifold expands into two conical regions symmetric about the origin, which morph into two 3-sided pyramidal shaped regions surrounding two symmetric stable equilibria with additional

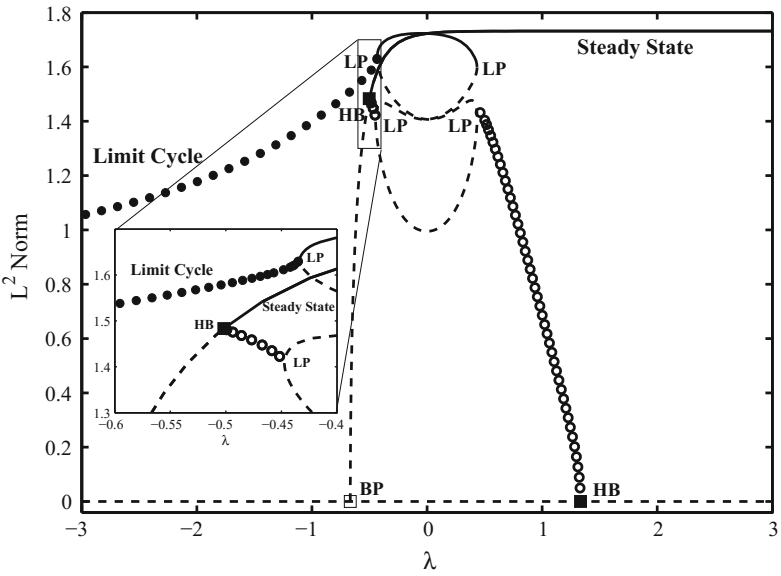

Fig. 2.7 Bifurcation diagram for a system of three identical bistable elements coupled unidirectionally and without delay. *Solid* (*dotted*) *lines* indicate stable (unstable) equilibrium points. *Filled-in (empty)* circles represent stable (unstable) periodic oscillations. (*Insert*) Close-up view of the region of bistability between large-amplitude oscillations and synchronous equilibria

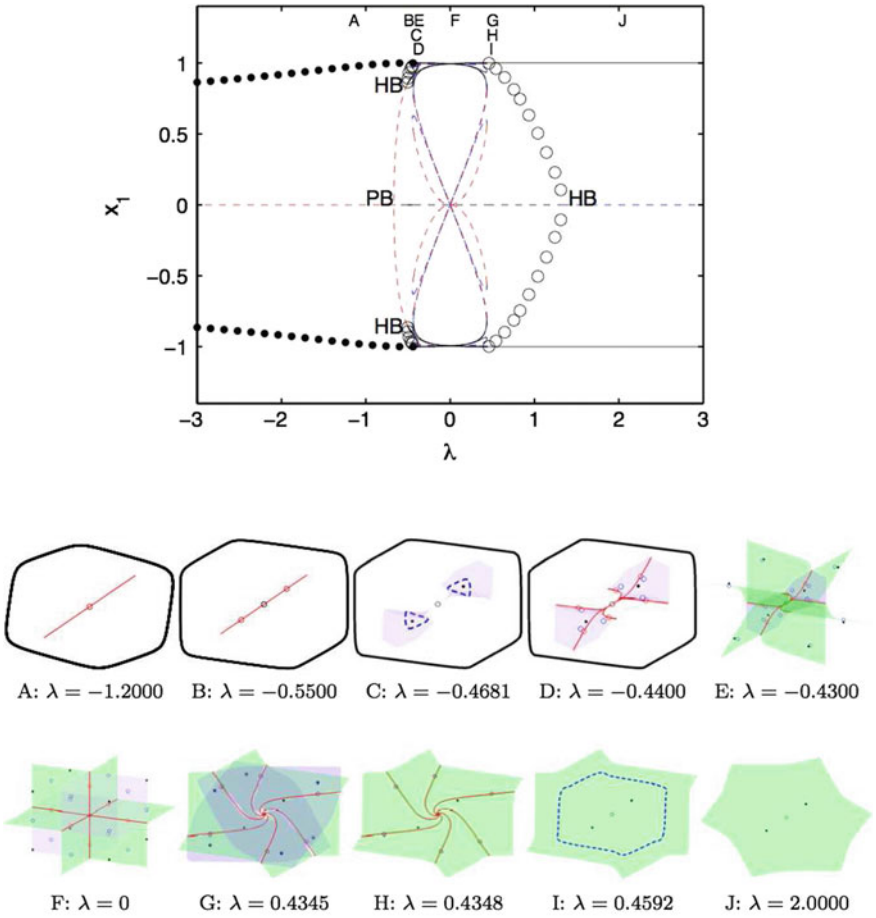

Fig. 2.8 Bifurcation diagram for system (2.7) computed in the equilibrium continuation program AUTO [101]. The diagram provides the values of x_1 at equilibria and the maximum and minimum values of x_1 at periodic orbits. Solid (*dashed*) lines indicate stable (unstable) equilibrium points. For unstable equilibria, *black (dashed)* indicates a 3D unstable manifold, *red (dashed)* has a 1D stable manifold, and *blue (dashed)* presents a 2D stable manifold. *Filled-in (empty)* circles represent stable (unstable) periodic oscillations. Parameters are $c = 3$ and $\epsilon = 0$. Notation: HB denotes Hopf bifurcation points and PB is a pitchfork bifurcation point

increases in λ. The 3-fold stable limit cycle has its period increase until it spends longer and longer times near six points, which appear as stable equilibria through a saddle node bifurcation. A second saddle node bifurcation produces six other asymmetric equilibria, which arise and generate separatrices. These divide our space into eight basins of attraction. Two are the small symmetric pyramidal shaped regions centered on the line $x_1 = x_2 = x_3$, while the other six attracting regions surround these symmetric regions.

As λ increases to zero, the uncoupled state, these eight basins of attraction shrink or expand until they become simply the eight octants in 3-space with stable equilibria near $x_i \approx \pm 1$ for $i = 1, 2, 3$. As λ becomes more positive, the two symmetric basins of attraction increase in size, while the six asymmetric basins shrink in size. Another saddle node bifurcation occurs with the loss of six stable equilibria in the six asymmetric basins of attraction, and the separatrices between these equilibria and the remaining symmetric equilibria vanish. The remaining 2D stable manifold (separatrix) with 3-fold symmetry divides our 3-space into two basins of attraction containing our only two remaining stable equilibria. Further increases in λ only result in a flattening of this separatrix between the symmetric stable equilibria.

Recall from Chap.1, Sect. 1.4, the definition of the group orbit of any point $x(t)$:

$$\Gamma x = \{\gamma x : \gamma \in \Gamma\}.$$

Thus, collectively, there are 27 equilibrium points, which can be arranged into one of four group orbits generated by the symmetry group $\Gamma \simeq \mathbf{Z_2^3} \otimes \mathbf{Z_3}$, see Fig. 2.9. Thus, Fig. 2.9 can be interpreted as a color-coded evolution of four distinct group orbits as a function of λ, which yields: a straight-line in the middle connecting the two symmetric equilibria $(\pm x, \pm x, \pm x)$ and the origin; six gray-to-black corner segments connecting six asymmetric stable nodes of the form $(\pm x, \pm x, \mp x)$; twelve blue curves for the group orbit of twelve asymmetric unstable nodes with representative $(0, \pm x, \pm x)$; six red curves which connect the remaining six asymmetric unstable saddle nodes of the type $(0, 0, \pm x)$. All other equilibria can be readily obtained by applying directly the 24-elements of the group Γ to the representative elements listed above. We observe in Fig. 2.9 that if one begins at any one of the asymmetric equilibria and increases and decreases λ between the saddle node bifurcation values, then one can continuously reach all the remaining 23 asymmetric equilibria.

Onset of Large Amplitude Oscillations. We now investigate the global bifurcation that leads to the onset of stable infinite-period oscillations, and seek an analytic expression for the critical point λ_c. It is well-known that a generic feature of symmetric nonlinear systems is the existence of *heteroclinic cycles*, defined as a collection of solution trajectories that connect sequences of equilibria and/or periodic solutions [239]. Heteroclinic cycles are highly degenerate. Certain symmetries, however, can facilitate the existence of cyclic trajectories that can "travel" through invariant subspaces while connecting, via saddle-sink connections, one solution to another. In Eq. (2.6), in particular, we find six near-invariant planar regions (with $\lambda < 0$):

$$\begin{aligned} \delta_i &= \{x_i : \lambda x_i < 1, \quad x_{(i+2 \bmod 3)} = -1\}, \quad i = 1, 2, 3, \\ \delta_i &= \{x_i : \lambda x_i > -1, \; x_{(i+2 \bmod 3)} = 1\}, \quad i = 4, 5, 6. \end{aligned}$$

Then the solution trajectories on the cycle lie on flow-invariant lines, see Fig. 2.10, defined by the intersection of the invariant planes. A typical trajectory on the cycle connects six saddle points located near the points: $(1, -1, -1)$, $(1, 1, -1)$, $(-1, 1, -1)$, $(-1, 1, 1)$, $(-1, -1, 1)$, and $(1, -1, 1)$.

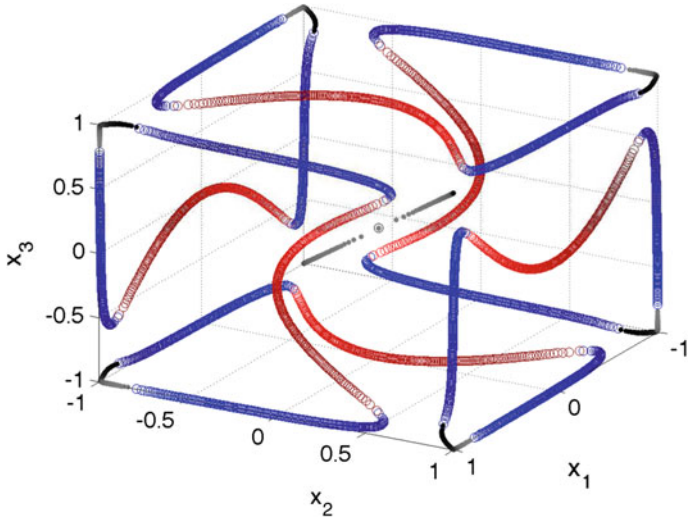

Fig. 2.9 There are 27 equilibria of Eq. (2.7) shown in this diagram at various values of λ. Three are the origin and the two symmetric equilibria. There are 24 asymmetric equilibria, which over the range of λ connect in a long chain. The *gray-black* equilibria are stable. The *blue* equilibria have 2D stable manifolds, and the *red* equilibria have 1D stable manifolds. The *darker the shade* of *blue* or *red* the higher the value of λ. Changes in color occur at saddle node bifurcations. A *gray-black* straight line for the graph of the group orbit of two symmetric equilibria, including the origin and three additional curves, *red*, *blue* and *gray*, for the 24 asymmetric equilibria

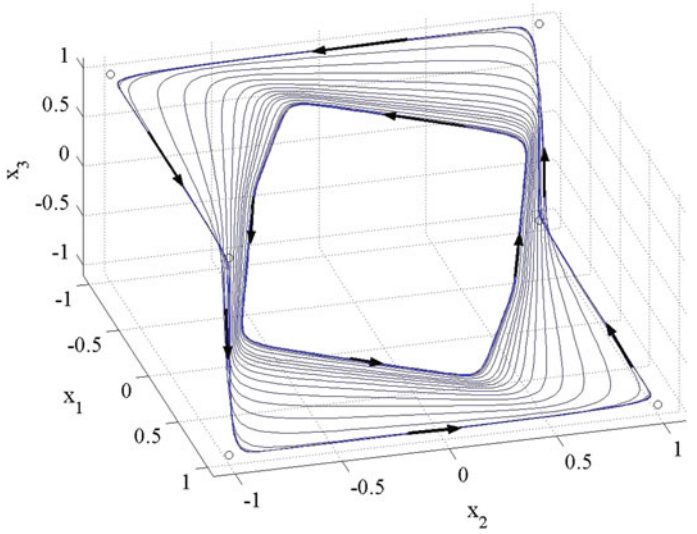

Fig. 2.10 Stable limit cycle solutions with amplitude $O(1)$ appear in system (2.6) for large negative values of λ. Fixed parameters are: $c = 3$, $\epsilon = 0$. *Arrows* indicate the direction of the flow

The saddle points exist only for $\lambda > \lambda_c$ and are annihilated when the periodic solutions appear. This suggests that we could determine the exact location of the heteroclinic cycle by finding the regions of parameter space where the saddle points exist, but leads to the complicated task of finding roots of polynomials of high order. On the other hand, we can use the fact that, at the birth of the cycle, solutions are confined to invariant lines. The flow on these lines cannot be obstructed by other equilibrium points, unless they are part of the cycles. This leads to the following conditions for existence of a cyclic solution:

$$-x + \tanh(c(x - \lambda + \epsilon)) > 0 \tag{2.8}$$

$$-x + \tanh(c(x + \lambda + \epsilon)) < 0. \tag{2.9}$$

When $\epsilon = 0$, the lhs of (2.8) and (2.9) each have a local minimum and a local maximum for $x \in (-1, 1)$. When $\epsilon > 0$, both extrema are shifted vertically. Thus, (2.8) is satisfied for $\epsilon = 0$ as well as $\epsilon > 0$. Hence, we only have to worry about condition (2.9). To find the critical point λ_c, we then compute the local maximum of (2.9), set it to zero, and solve for λ. We get:

$$\lambda_c = -\epsilon + \frac{1}{c}\ln(\sqrt{c} + \sqrt{c-1}) - \tanh(\ln(\sqrt{c} + \sqrt{c-1})). \tag{2.10}$$

An alternative derivation shows that this critical value of coupling strength can be expressed as

$$\lambda_c = -\varepsilon - x_{inf} + c^{-1}\tanh^{-1} x_{inf},$$

with $x_{inf} = \sqrt{(c-1)/c}$ is the inflection point of the energy function

$$U(x) = \frac{x^2}{2} - T\ln\left(\cosh\left(\frac{x+h}{T}\right)\right).$$

To verify this result, we conducted, numerically, a two-parameter continuation analysis using AUTO with $c = 3$, see Fig. 2.11. The dark diagonal line represents the loci of the heteroclinic cycle obtained numerically by AUTO, which shows very good agreement with the analytic loci determined by (10.49) (superimposed square points). The other curves represent the loci of HB points, which in all cases lead to unstable periodic solutions.

Generalization to Larger Networks. For larger odd values of N, and still unidirectional coupling amongst nearest neighbors, the system dynamics is more complicated than in the previous case with $N = 3$. For $N = 5$, for instance, three additional branches of periodic solutions are created via local Hopf bifurcations (the bifurcation diagrams are omitted for brevity). One branch is created off the trivial solution, $x_1 = \ldots = x_5 = 0$, while the other two emerge from the non-trivial steady-states. All Hopf branches are unstable, so that the only *observable* oscillatory behavior still originates from the heteroclinic cycle—as it happens in the $N = 3$ case. This also

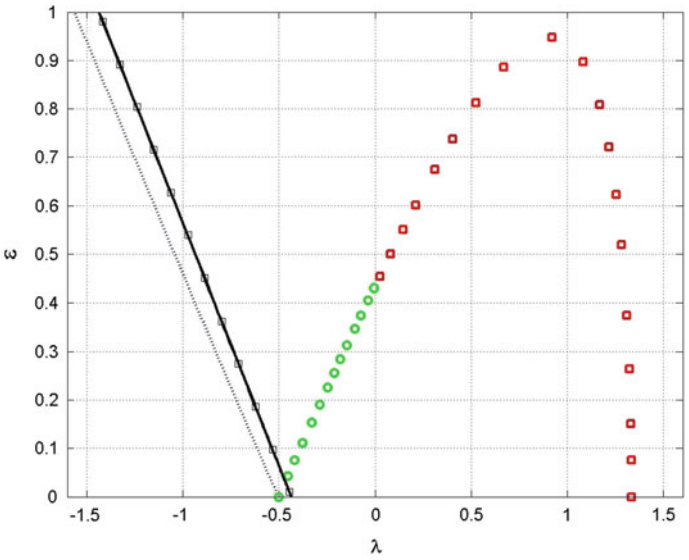

Fig. 2.11 Two-parameter continuation of Hopf bifurcation points *(dash line, empty circles, and squares)* and heteroclinic connections (*black line* obtained numerically via AUTO, superimposed *squares* obtained analytically). Periodic solutions are globally stable only for parameter values (λ, ϵ) below the *black line*, and unstable everywhere else. The temperature-related parameter is $c = 3$

holds true for larger odd values of N except that as N increases, the amplitude of the observable oscillations asymptotically approaches unity and more branches of unstable periodic solutions bifurcate from the non-zero steady-state.

For even values of N, and preserving uni-directional coupling between nearest-neighbors, the system also undergoes a series of Hopf bifurcations, but all of the branches are unstable and, hence, unobservable. Figure 2.12 shows representative examples for $N = 4$ and $N = 6$.

As $N \to \infty$, these unstable solutions differ by a vanishingly small amount with those unstable solutions found with N odd. Geometrically, the two chains of cyclic subgroups of symmetries given by

$$\mathbf{Z}_3 \subset \mathbf{Z}_5 \subset \mathbf{Z}_7 \subset \ldots$$
$$\mathbf{Z}_4 \subset \mathbf{Z}_6 \subset \mathbf{Z}_8 \subset \ldots$$

become increasingly closed to one another and the degree of instability of each unstable branch of periodic solutions weakens. In the limit, $N = \infty$, the cyclic ring becomes a continuous ring with circular $\mathbf{O}(\mathbf{2})$ symmetry. The solutions of this continuous system are then determined by the theory of $\mathbf{O}(\mathbf{2})$-Hopf symmetry-breaking bifurcation.

While more specialized coupling schemes are beyond the purview of this book, we have also investigated different coupling topologies that include: bidirectional

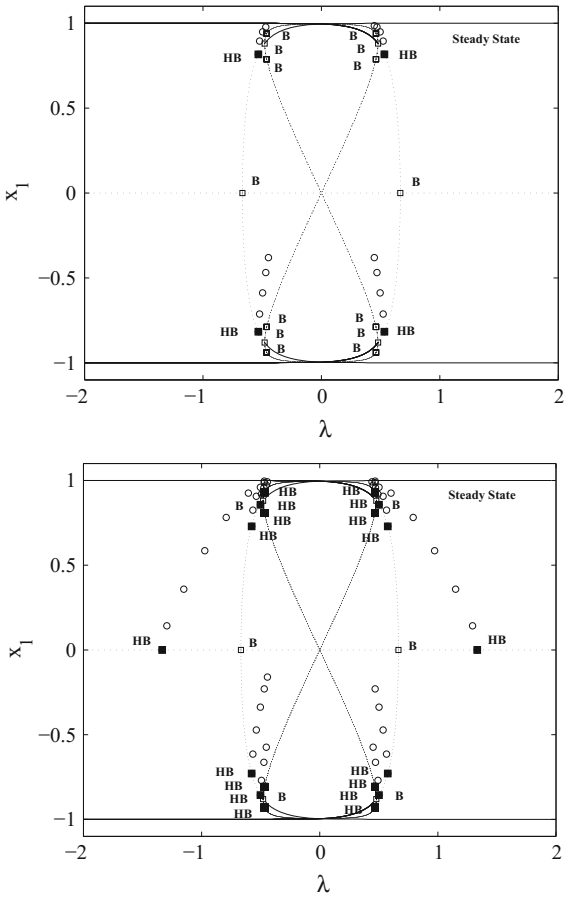

Fig. 2.12 Bifurcation diagram for a coupled-fluxgate system similar to that used in Fig. 2.7, except for larger even values of N. All branches of periodic solutions *(empty circles)* are unstable. The *dotted curves* (part of the figure-8 loop) represent the unstable steady state solutions. $N = 4$ (*top*) and $N = 6$ (*bottom*)

coupling amongst nearest neighbors, unidirectional coupling for nearest neighbors combined with bidirectional coupling between non-nearest neighbors, and unidirectional coupling for nearest neighbors combined with unidirectional coupling between every other non-nearest neighbors. It is worth mentioning that additional coupling facilitates the existence of oscillatory behavior but aside from a potential enhanced tolerance to background noise, increasing the number of elements or re-arranging the network to have a different coupling topology does not seem to increase performance as quantified, for example, by the sensitivity of the oscillation frequency to small changes in an applied dc target signal. However, different coupling topologies (e.g. bidirectional coupling) may help reduce the effective noise floor of the system, thereby affording the device some additional sensitivity. These issues will be addressed in future work. In summary, from the application point of view, the $N = 3$ case, as presented in [195] and in this book, is the simplest, and most relevant, case to realize.

2.4 Frequency Response

The oscillation frequency ω, as a function of the system parameters, can be calculated from its period T. Near the onset λ_c of oscillations, T is essentially the time required for a solution to travel along the invariant lines of the heteroclinic cycle. By symmetry, the time spent on each branch is approximately the same. Hence, $T \approx 6\int_{-1}^{1} dt$, where $dt \approx dx/(-x+\tanh(c(x-\lambda+\epsilon)))$, and the integral must be evaluated numerically. In Fig. 2.13, we examine the relation between frequency and system parameters λ and ϵ with $c = 3$. The zero-frequency line in the $(\lambda,\ \epsilon)$ plane is in very good agreement with our expression (10.49) for the critical coupling strength.

Then a numerical approximation (for the special case of $N = 3$) for the frequency dependence on the system parameters can be obtained:

$$\omega = 0.115\sqrt{-\lambda - 0.85\epsilon - 0.4345}. \tag{2.11}$$

As mentioned earlier, the oscillations are not sinusoidal, however, they tend to being sinusoidal for large coupling strength magnitude ($\lambda \ll \lambda_c$; recall that $\lambda_c < 0$). It was, further, observed that the sum $X(t) = \sum_i x_i(t)$ could be a useful quantity for device applications; the period of the summed response was seen to be T_i/N, where T_i is the period of individual oscillations in an N-coupled ring. Finally, we note that the individual responses $x_i(t)$, while having the same frequency (assuming that the

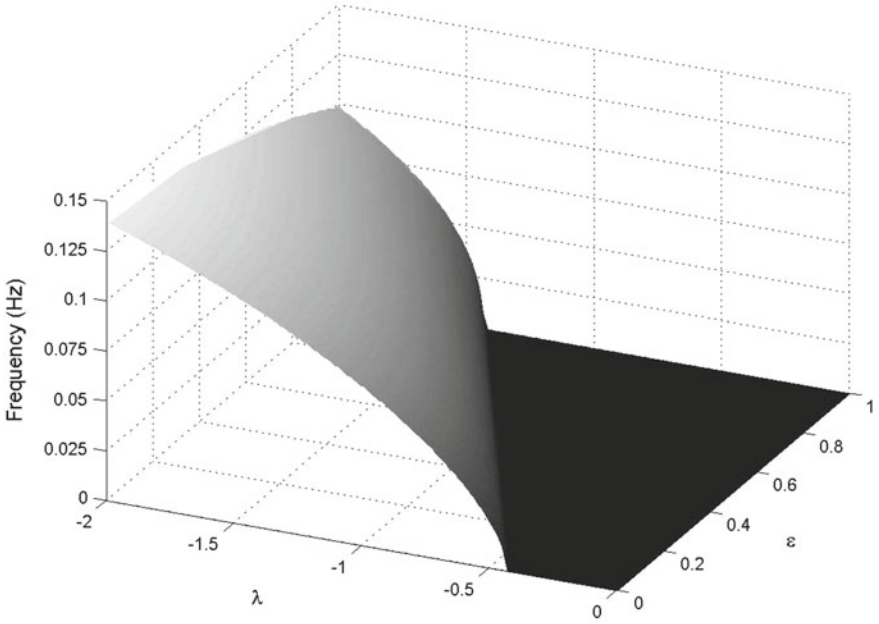

Fig. 2.13 Frequency response versus system parameters λ and ϵ, for coupled system (2.6) with $N = 3$ and $c = 3$

parameters c and λ are the same throughout the dynamics (2.6)), are offset in phase by $2\pi/N$. Increasing N leads to different frequencies for the individual elements $x_i(t)$, with a concomitant phase difference between solutions; however, the summed response has a frequency that is *independent* of N, as long as the other parameters c and λ remain unchanged. This will become apparent in what follows. Figure 2.14 shows the oscillations and the summed response in the system (2.6), and different values of the coupling strength λ and dc asymmetrizing signal ε. The top panel shows the oscillations near the critical point. Summed response is indicated by thick black lines, and individual element responses follow the gray lines in all panels.

Typical of the heteroclinic cycles, the amplitudes are fully grown at the start of the bifurcation and the frequency is low. At the birth of the oscillations, the frequency is zero as predicated by the heteroclinic bifurcation. The parameters are set

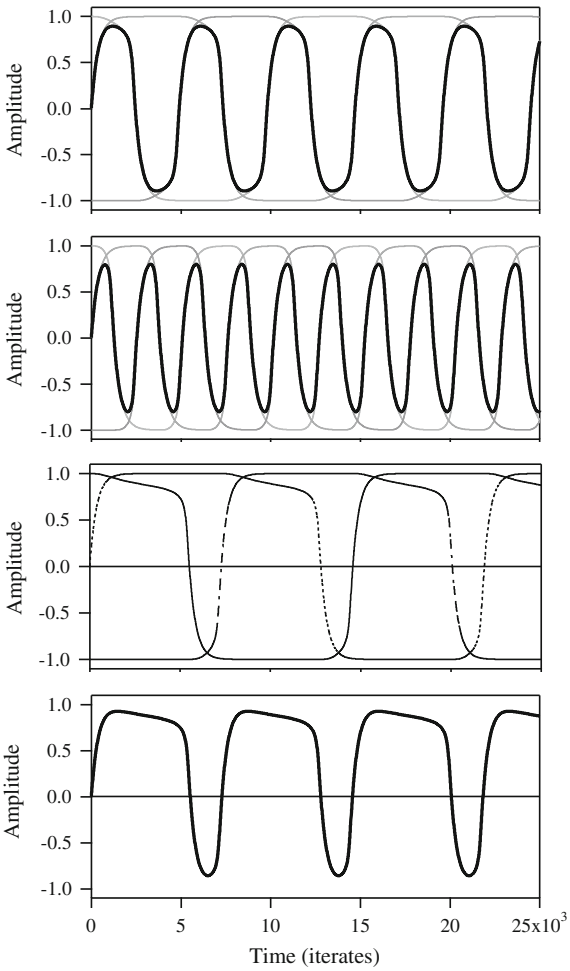

Fig. 2.14 Emergent oscillatory behavior in the coupled system (2.6) for $N = 3$. Initial conditions are $(x_1, x_2, x_3) = (1.0, 0.0, -1.0)$, $c = 3$. *Top panel* shows the oscillations near the critical point. Summed response is indicated by thick *black lines* in all panels. The *second panel* shows the oscillations for a higher coupling strength $\lambda = -0.75$, and $\varepsilon = 0$. The *third panel* shows the oscillations for $\lambda = -0.60$, $\varepsilon = 0.05$. Notice that the sum signal (last panel) is greatly offset between the upper state (above zero) and the lower state (below zero)

at $\lambda = -0.60, \varepsilon = 0$. The second panel shows the oscillations for a higher coupling strength $\lambda = -0.75$, and $\varepsilon = 0$. Contrasted with the top panel, the frequency increases significantly. The frequency scales as a square root of λ and ε. The third panel shows the individual element oscillations for $\lambda = -0.60, \varepsilon = 0.05$. Notice that the sum signal (last panel), corresponding to the individual oscillations in the third panel, is greatly offset between the upper state (above zero) and the lower state (below zero). Also notice the decrease in frequency when the target signal ε is non-zero compared to the top panel.

Next we develop a more detailed description of the system dynamics. In particular, we derive an expression for the oscillation period in terms of the separation $\lambda_c - \lambda$ (recall that $\lambda, \lambda_c < 0$ in the convention adopted in (2.6), so that the separation is a positive quantity for $\lambda < \lambda_c$). We also obtain expressions for the time spent in each of the two stable attractors of the potential energy functions that describe the individual elements in (2.6) in the absence of coupling.

2.5 Sensitivity Response

Residence Times Detection. Our new sensing technique, the *Residence Times Detection*, consists of measuring the "residence times" of the oscillations of the sensor device about the two stable states of the potential energy function $U(x)$. In the absence of noise and of external signals, the potential energy function is symmetric; hence, the two residence times are identical, i.e., $T_+ = T_-$. In the presence of a target signal, however, the hysteresis loop is skewed and the crossing-times are no longer equal. Then either the difference $|T_+ - T_-|$ or the ratio T_+/T_- of residence times can be used to quantify the signal, see Fig. 2.15. In the presence of noise, the residence times must be replaced by their ensemble averages.

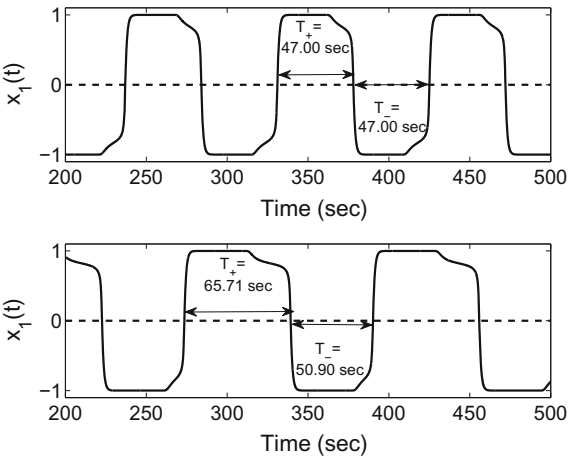

Fig. 2.15 Residence Time Detection. (*Top*) Without an external field, i.e., $\varepsilon = 0$, the wave form has *top-to-bottom* symmetry. (*Bottom*) With an external field, $\varepsilon = 0.01$ in this case, the wave forms develops an asymmetry. Then the difference or ratio of crossing times can used to quantify the external signal

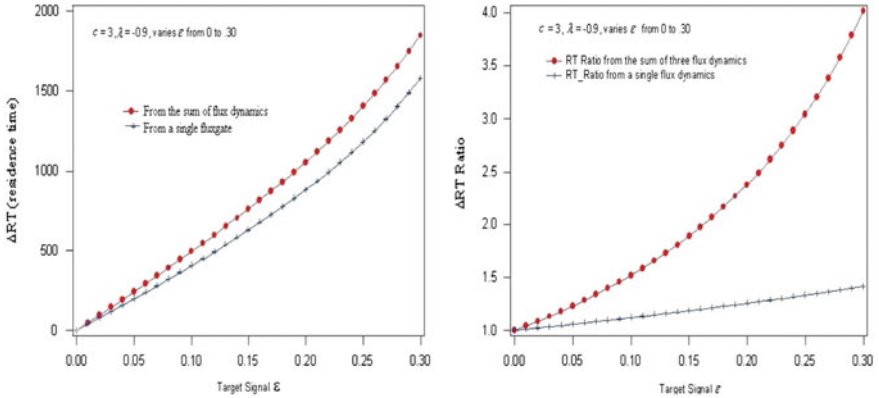

(a) RT Difference (b) RT Ratio

Fig. 2.16 Signal detection via residence time *left* differences and *right* ratios

Advantages of this procedure are: it can be implemented on-chip without the computationally demanding power spectral of the system output; large-period oscillations yield large differences/ratios of residence times, i.e., better sensitivity; it can be optimized to require very low onboard power.

Numerical simulations show that, near the onset point λ_c, the period of the summed waveform becomes very large, which causes the waveform to yield larger values of the RT difference/ratio when an external signal is present, i.e., higher sensitivity. For illustrative purposes, Fig. 2.16 compares the theoretical sensitivity of a single fluxgate with that of a network of $N = 3$ sensors. The slope of a RTD curve is proportional to the level of sensitivity. It follows that a network of three fluxgates with RTD ratio readout can be, approximately, 200 times more sensitivity than a single fluxgate.

We now turn to a more analytical description of the sensitivity response through the dynamics of (2.14), confining ourselves to the immediate neighbourhood of the critical point in the oscillatory regime, i.e., when the separation $\lambda_c - \lambda$ is small. We note, however, that our results provide a very good description of the dynamics (in particular, the scaling of the oscillation period with the coupling strength and/or symmetry-breaking signal) well past the onset of the oscillations; this will become apparent later in this section. We carry out the analysis for $N = 3$ elements, with the generalization to arbitrary N made clear at the end. We refer to Fig. 2.14, specifically the third and fourth panels which correspond to the case of small separation $\lambda_c - \lambda$. Note that Fig. 2.14 was generated using a specific set of initial conditions, however, the analysis will make clear that the dynamics evolve independently of this choice, as long as at least one element has an initial state different from the others.

For small separation $\lambda_c - \lambda$, it is clear that the state-points spend the bulk of their transition times reaching the inflexion points $\pm x_{inf} = \pm\sqrt{(c-1)/c}$, after

which the passage to the opposite minimum (at ± 1) is very rapid. Put differently, the combination of dc and coupled fluxes in each of the elements of (2.6), cause that particular potential to skew or tilt so that a minimum and the saddle point approach each other, coalescing into an inflection point. At this point, an infinitesmial further tilt, causes the state-point to drop into the opposite minimum, all the time providing an input to the next (forward-coupled) element via the coupling, so that a soliton-like periodic disturbance travels around the ring. One also notes that the elements evolve two at a time, with one element always remaining in its steady state while the others evolve. This behavior is reminiscent of what might be expected in a discrete line of magnetic spins, subject to a dc magnetic field. For an odd number of spins, there will always be two spins that have the same alignment, and are therefore "frustrated", with each spin trying to orient itself anti-parallel to the other.

It is also clear that the zero crossing points $t_0(=0), t_1, t_2$ etc. of the summed output $X(t)$ also correspond to the crossing points of the individual elements e.g.t_1 corresponds to the zero-crossing of $x_1(t)$, t_2 for $x_3(t)$, etc. Hence, the problem of finding the period T_+ of the summed output, or the individual oscillation periods $T_i \equiv T_3$ (which are all the same; the suffix refers to the $N = 3$ case) reduces to determining the zero-crossing times $t_{1,2}(t)$.

From our discussion above it is evident that, during the dominant part (in Fig. 2.17 this corresponds to the half-cycle starting at $x_1 = 1$) of the evolution of $x_1(t)$, the element $x_2(t)$ remains in its steady state $x_+ \approx 1$ (the exact locations of the fixed points can be readily found via simple calculus, as has been done in [60], and for $c > 1$ are very close to ± 1, due to the tanh function) so that the first of the Eq. (2.6) can be simplified to:

$$\dot{x_1}(t) = -x_1 + \tanh c(x_1 + \lambda + \varepsilon), \tag{2.12}$$

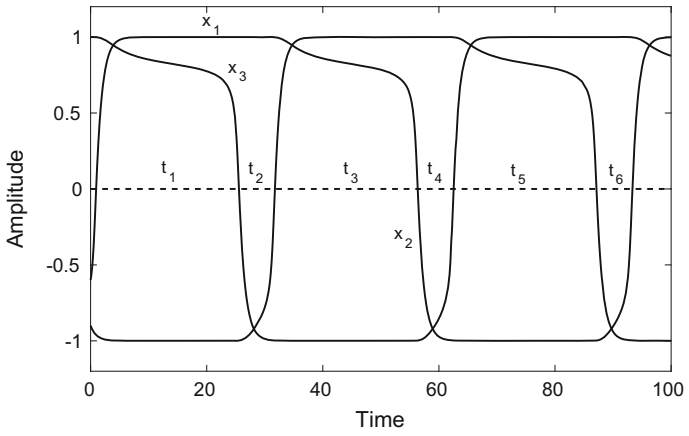

Fig. 2.17 Time series simulations of a CCFM (Coupled-Core Fluxgate Magnetometer) system. Time *intervals* t_i are used (see text) in the calculation of the period and RTD. Parameters are: $N = 3$ cores, $c = 3$, $\lambda = -0.54$, and $\epsilon = 0.07$

corresponding to simple "particle-in-potential" motion. Formally integrating this equation yields,

$$t_1 = \int_1^0 \frac{dx_1}{\tanh c(x_1 + \lambda + \varepsilon) - x_1}, \tag{2.13}$$

where t_1 is the time taken (for this choice of initial conditions) by the state-point $x_1(t)$ to evolve from its attractor at $+1$, to 0 (Fig. 2.14). This integral cannot be evaluated analytically, in general. Similarly, we see that $x_3(t)$ evolves while $x_1(t) \approx -1$ so that we have

$$\dot{x_3}(t) = -x_3 + \tanh c(x_3 - \lambda + \varepsilon), \tag{2.14}$$

whence we obtain,

$$t_{12} \equiv t_2 - t_1 = \int_{-1}^0 \frac{dx_3}{\tanh c(x_3 - \lambda + \varepsilon) - x_3}. \tag{2.15}$$

From these two integrals, we may write down the period T_+ of the summed output as $T_+ = t_{12} + t_1$ by formally summing the above expressions. A little manipulation of the integration limits shows immediately that $T_+ = 2t_1$ for $\varepsilon = 0$, as expected. Having obtained the above expressions, it is easy to see that $t_3 = T_+ + t_1$, $t_4 = 2T_+$, $t_5 = 2T_+ + t_1$, $t_6 = 3T_+$, etc. In particular, we can write down the expression for the individual periods as $T_3 = 3T_+$, and for the phase differences between individual solutions as $t_3 - t_1 = t_5 - t_3$ etc., so that the phase difference is $2\pi/3$.

The generalization of the above observations to arbitrary N should now be clear. In this case, the individual periods (and the phase offsets) do change; however, again, only two elements are simultaneously evolving at any given time, the remainder staying in their steady states. Hence, the period of the summed output is always the same, and we obtain, $T_+ = T_i/N$ where T_+ is now the summed output of N (odd) elements, and T_i is the period of the individual oscillations for the $i = N$ case. The phase offset between solutions for arbitrary N is $2\pi/N$. It is worth noting that increasing N leads to a concommitant increase in the period of the individual oscillations. A similar result was obtained in a globally coupled network of dc SQUIDs [3] whose individual elements could undergo saddle-node bifurcations to oscillatory behavior in the absence of the coupling.

Referring now to the summed output $X(t)$, the difference in zero-crossing times is a direct marker of the asymmetrizing target signal ε. We write this as $\Delta t = t_1 - t_{12}$ which, after some manipulations can be written as,

$$\Delta t = \int_0^1 dx \left[\frac{1}{\tanh c(x + \lambda - \varepsilon)} - \frac{1}{\tanh c(x + \lambda + \varepsilon)} \right], \tag{2.16}$$

which, for small ε may be written as,

$$\Delta t \approx 2c\,\varepsilon \int_0^1 dx \frac{sech^2 c(x + \lambda)}{[\tanh c(x + \lambda) - x]^2}. \tag{2.17}$$

This result shows that Δt is proportional to ε for small (compared to the energy barrier height) target signals, a result that has already been quantified [60] in single fluxgate magnetometer experiments. In this regime, we may define a sensitivity S via the derivative $\partial \Delta t / \partial \varepsilon$, yielding an expression that is independent of ε. For a practical system, this is a desirable result. It is also obvious that the RTD and the associated sensitivity would be the same if we chose to compute them via the zero-crossings of any one of the solutions $x_i(t)$, rather than the sum. Note, also, that the oscillations shown in Fig. 2.14 are *supra*threshold, an important point, since it mitigates the effect of noise and allows a "natural" operation with an effectively suprathreshold bias signal; by contrast, we point to the $N = 1$ case [60] wherein the oscillations were generated on-board the (single) device through an external source with controllable amplitude and frequency. Note that, theoretically at least, the optimal operating point for a single bistable device corresponds to a bias signal that is slightly *sub*threshold [291]. In this regime, a combination of the signal and background noise induce hopping between the stable steady states of the potential. However, practical issues, e.g. the longer observation times required in the presence of a non-negligible noise background, often preclude operation in this regime.

It is easy to plot the quantities expressed via the formal integrals (2.13) and (2.15); before doing so, however, we derive analytic expressions for the period T_+ when the separation $\lambda_c - \lambda$ is very small. We note that the procedure of this section starts to break down when $|\lambda|$ increases signifiantly past $|\lambda_c|$, because the approximation of assuming that the elements evolve only two at a time with the rest of them remaining fixed at their (constant) steady state values throughout the evolution, becomes increasingly tenuous, and we can no longer replace the coupling factors (inside the nonlinearities) by constants. This is evident from the right panels of Fig. 2.14. For this situation, one must compute the period via direct integration of the original coupled system (2.6), although qualitative behavior can still be very well predicted using the approximate theory.

The integrals in (2.13) and (2.15) may be evaluated just past the critical point, where the integrands display sharply peaked behavior. We start with (2.13) and note that the denominator is sharply peaked at $x = x_m$, a value that can be found by differentiation as $x_m = -\lambda - \varepsilon + (1/c)\tanh^{-1} x_{inf}$ where $x_{inf} = \sqrt{(c-1)/c}$ denotes the location of the point of inflexion. The critical coupling at which the potential function corresponding to the x_1 dynamics has an inflexion point, may be obtained by setting $f(x_{inf}, \lambda_c) = 0$, $f(x, \lambda)$ being the denominator in the integrand of (2.13). We readily obtain,

$$\lambda_c = -\varepsilon - x_{inf} + \frac{1}{c}\tanh^{-1} x_{inf}, \tag{2.18}$$

so that $x_m = \lambda_c - \lambda + x_{inf}$. We now expand the denominator $f(x)$ about $x = x_m$ obtaining, after some algebra,

$$f(x) \equiv \tanh c(x + \lambda + \varepsilon) - x \approx \lambda - \lambda_c - c x_{inf}(x - x_m)^2. \tag{2.19}$$

Then, finally, we can evaluate the integral in (2.13), extending the limits to $\pm\infty$ (because of the sharply peaked nature of the integrand):

$$t_1 \approx \int_{-\infty}^{\infty} \frac{dx}{\lambda_c - \lambda + cx_{inf}(x - x_m)^2} = \frac{\pi}{\sqrt{cx_{inf}}\sqrt{\lambda_c - \lambda}}. \tag{2.20}$$

In an analogous way, we can develop a closed form expression for the integral in (2.15):

$$t_{12} \approx \int_{-\infty}^{\infty} \frac{dx}{\lambda_c - \lambda + 2\varepsilon + cx_{inf}(x - x_{mm})^2} = \frac{\pi}{\sqrt{cx_{inf}}\sqrt{\lambda_c - \lambda + 2\varepsilon}}, \tag{2.21}$$

where $x_{mm} = \lambda - \varepsilon - \frac{1}{c}\tanh^{-1} x_{inf}$. The oscillation period T_+ of the summed response is then obtained by summing the last two expressions to yield

$$T_+ = \frac{\pi}{\sqrt{cx_{inf}}}\left[\frac{1}{\sqrt{\lambda_c - \lambda}} + \frac{1}{\sqrt{\lambda_c - \lambda + 2\varepsilon}}\right]. \tag{2.22}$$

A comparison between the angular frequency obtained from this expression and from direct numerical simulations is presented in Figs. 2.18 and 2.19. This comparison shows that the analytical expression captures the dynamics well, especially near the bifurcation threshold, but also well into the oscillating regime. This is attributable to the fact that the peaked nature of the denominators of (2.13) and (2.15) persists well into the oscillating regime, even though the peaks get broader as one moves deeper into this regime.

In the immediate vicinity of the critical point, i.e., $\lambda_c - \lambda$ is positive and small, we may approximate the period of the summed oscillation by (2.22), which displays the inverse square-root scaling behavior that one should expect. Note that $\lambda_c = \lambda_c(\varepsilon)$ which leads to $T_+ = 2t_1$ in the absence of the asymmetrizing signal ε. This behavior is captured in Fig. 2.20 where we plot the angular frequency obtained by direct

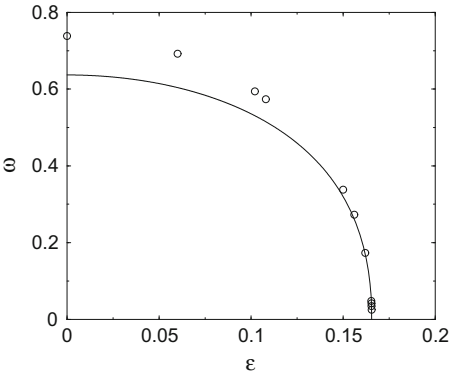

Fig. 2.18 The angular frequency of the summed response calculated via direct numerical simulations (*solid line*), and via the approximate relationship in Eq. 2.22. Parameter values are: $N = 3$, $c = 3$ and $\lambda = -0.6$, giving $\varepsilon_c \sim 0.1656$

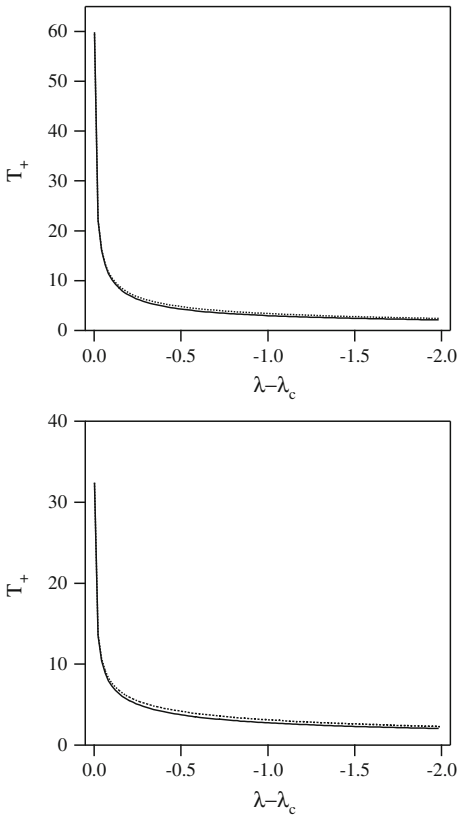

Fig. 2.19 Period T_+ of the sum signal obtained via numerical simulation of the dyanmics (2.6) *(solid curve)*, and via the expression (2.22). *Top* $c = 4$, $\varepsilon = 0$. *Bottom* $\varepsilon = 0.2$. The approximation agrees very well with the numerically obtained period, even for large λ and ε

integration of the dynamics (2.6), versus the approximation (2.22). It is seen that (2.22) provides a good answer everywhere, but especially for very small separations $\lambda_c - \lambda$. It is worth noting that we can carry out a small-ε expansion for the period:

$$T_+ \approx \frac{\pi}{cx_{inf}} \frac{1}{\sqrt{\lambda_{c0} - \lambda}} \left[2 + \frac{3}{4} \left(\frac{\varepsilon}{\lambda_{c0} - \lambda} \right)^2 + O(\varepsilon^4) \right] = T_{+0} + const.\varepsilon^2, \quad (2.23)$$

which is valid for $\varepsilon \ll \lambda_c - \lambda$, with $\lambda_{c0} = -x_{inf} + (1/c) \tanh^{-1} x_{inf}$ the critical coupling for the onset of oscillations in the absence of the asymmetrizing signal.

The approximations to the times t_1 and t_{12} lead, directly, to an approximate expression for the RTD $\Delta t (= t_1 - t_2)$ close to the critical point:

$$\Delta t \approx \frac{\pi}{\sqrt{cx_{inf}}} \left[\frac{1}{\sqrt{\lambda_c - \lambda}} - \frac{1}{\sqrt{\lambda_c - \lambda + 2\varepsilon}} \right], \quad (2.24)$$

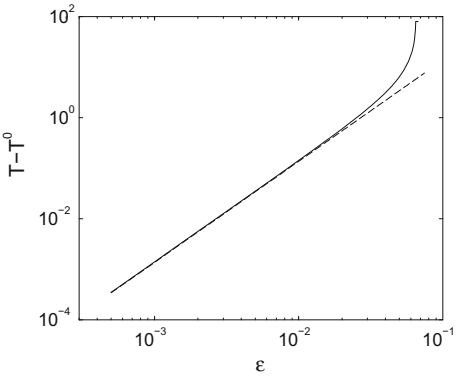

Fig. 2.20 The period T_+ of the summed oscillation, reduced by the period for $\varepsilon = 0$, as a function of ε. The results from the Taylor expansion (2.23) are plotted as a dashed line while the results from the direct numerical calculation are plotted as a *solid line*. The curve obtained via the expression (2.22) is indistinguishable from the *solid curve* at this scale. $N = 3$, $c = 3$, $\lambda = -0.5$

which also exhibits the square root behavior. Using the last expression, we can obtain an $O(\varepsilon)$ approximation to the RTD:

$$\Delta t \approx \frac{\pi\varepsilon}{\sqrt{cx_{inf}}}(\lambda_{c0} - \lambda)^{-3/2}, \tag{2.25}$$

so that the sensitivity $\partial\Delta t/\partial\varepsilon$ is enhanced as we get closer to the critical point, where we note that decreasing the temperature-dependent control parameter c close to unity, can also lead to enhanced sensitivity to small ε, as readily apparent in (2.25). It is worth pointing out that a sensitivity $\partial T_+/\partial\varepsilon$, defined via the oscillation period, is actually a function of ε. This may not be desireable in practical sensors where one would like to develop the optimal sensor configuration independently of the target signal. From this standpoint, the RTD may constitute the more reliable measure. Note also that when ε becomes comparable to the separation $\lambda_c - \lambda$, the expansions (2.23) and (2.25) do not agree well with simulations. This is apparent in Fig. 2.20, where we have plotted $T_+ - T_{+0}$ using direct numerical simulations and the expansion (2.23) as a function of ε.

2.6 Alternating Configuration

Laboratory experiments seem to indicate that the sensitivity of a Coupled Core Fluxgate Magnetometer or CCFM-based system of fluxgates increases by simply alternating the orientation of each individual fluxgate. We call this new arrangement a CCFM system with *Alternating Orientation* (AO). We should clarify that the coupling scheme remains the same, i.e., unidirectional coupling via induction. The only

feature that changes is the direction at which the individual fluxgates are aimed for signal detection purposes. Thus the sign in front of the target signal ε alternates between $+$ and $-$ so that the governing equations (for the deterministic system) become,

$$\dot{x}_i = -x_i + \tanh(c(x_i + \lambda x_i + (-1)^{i+1}\varepsilon)),\ i = 1, \ldots, N \bmod N. \tag{2.26}$$

Next we calculate the region of existence of stable coupling-induced oscillations using the ideas and methods from our previous work on the analysis of the standard CCFM configuration [195]. Direct calculations (similar to the standard orientation) yield

$$\lambda_c^{AO} = -\epsilon + \frac{1}{c}\ln(\sqrt{c} + \sqrt{c-1}) - \tanh(\ln(\sqrt{c} + \sqrt{c-1})). \tag{2.27}$$

Equation (2.27) describes the onset of oscillations in the CCFM system with AO configuration. This onset is exactly the same as that of the standard configuration. Interestingly, the AO configuration does not change the two-parameter region where stable coupling-induced oscillations exist. More interesting, however, is the fact that the sensitivity response of the AO configuration does change. Actually, it improves significantly in our experimental observations, a claim that we now approach analytically. We do so by calculating the RTD response of an AO configuration with the aid of time-series simulations of typical solution trajectories for $x_i(t)$; these solutions are shown in Fig. 2.21.

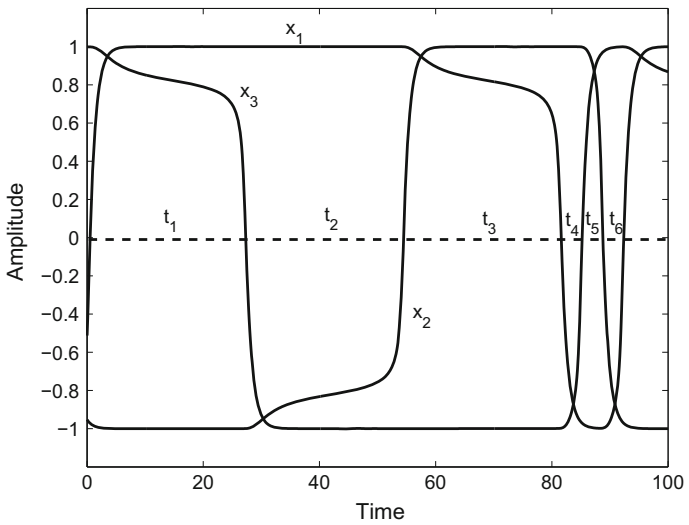

Fig. 2.21 Time series simulations of a CCFM system with cores oriented in an alternating fashion. Parameters are: $N = 3$ cores, $c = 3$, $\lambda = -0.54$, and $\epsilon = 0.07$. The time *intervals* t_i are used (see text) in the calculation of the period and RTD

From Fig. 2.21, we observe that on the interval t_1 the dominant part of $x_3(t)$ decreases from 1 (the approximate location of the fixed point of the "local" potential $U(x_1)$) absent any coupling) to 0 (the maximum of the local potential) while the element $x_1(t)$ remains in its steady state $x_+ \approx 1$ (the exact locations of the stable fixed points of each local potential can be readily found via simple calculus [195] and, for $c > 1$, are very close to ± 1, due to the tanh function) so that the last of the Eq. (2.26) (with $N = 3$) can be simplified to:

$$\dot{x_3}(t) = -x_3 + \tanh c(x_3 + \lambda + \varepsilon), \tag{2.28}$$

corresponding to simple "particle-in-potential" motion. It is important to note that, because of the sequential nature of the switching process one can reduce the dynamics to a description in terms of a "local" potential, even though the 3-variable coupled system cannot be described by a potential energy function. Formally integrating this equation yields,

$$t_1 = \int_1^0 \frac{dx_3}{\tanh c(x_3 + \lambda + \varepsilon) - x_3}, \tag{2.29}$$

where t_1 is the time taken (for this choice of initial conditions) by the state-point $x_3(t)$ to evolve from its stable attractor at $+1$, to 0 (Fig. 2.21). This integral cannot be evaluated analytically, in general. However, it may be evaluated just past the critical point (i.e. in the regime of low oscillation frequency), where the integrand is sharply peaked. We note that the denominator is sharply peaked at $x_3 = x_{m3}$, a value that can be found by differentiation as $x_{m3} = -\lambda - \varepsilon + (1/c)\tanh^{-1} x_{inf}$, where $x_{inf} = \sqrt{(c-1)/c}$. The critical coupling at which the potential function $U(x_3)$ corresponding to the x_3 dynamics has an inflection point, may be obtained by setting $f(x_{inf}, \lambda_{c3}) = 0$, $f(x, \lambda)$ being the denominator in the integrand of (2.29). We readily obtain,

$$\lambda_{c3} = -\varepsilon - x_{inf} + \frac{1}{c}\tanh^{-1} x_{inf}, \tag{2.30}$$

so that $x_{m3} = \lambda_{c3} - \lambda + x_{inf}$. We now expand the denominator $f(x_3)$ about $x_3 = x_{m3}$ obtaining, after some algebra,

$$f(x_3) \equiv \tanh c(x_3 + \lambda + \varepsilon) - x_3 \approx \lambda - \lambda_{c3} - c x_{inf}(x_3 - x_{m3})^2. \tag{2.31}$$

Then, finally, we can evaluate the integral in (2.29), extending the limits to $\pm\infty$ (because of the sharply peaked nature of the integrand):

$$t_1 \approx \int_{-\infty}^{\infty} \frac{dx_3}{\lambda_{c3} - \lambda + c x_{inf}(x_3 - x_{m3})^2} = \frac{\pi}{\sqrt{c x_{inf}}\sqrt{\lambda_{c3} - \lambda}}. \tag{2.32}$$

Next we calculate the interval t_2. Figure 2.21 shows that, on t_2, the dynamics along $x_2(t)$ changes while $x_3 \approx -1$ so that

$$\dot{x_2}(t) = -x_2 + \tanh c(x_2 - \lambda - \varepsilon), \tag{2.33}$$

which yields

$$t_2 = \int_{-1}^{0} \frac{dx_2}{\tanh c(x_2 - \lambda - \varepsilon) - x_2}. \tag{2.34}$$

Proceeding as in the t_1 case, we find that t_2 is, approximately, given by

$$t_2 \approx \int_{-\infty}^{\infty} \frac{dx_2}{\lambda_{c2} - \lambda + cx_{inf}(x_2 + x_{m2})^2}, \tag{2.35}$$

It can be shown that $x_{m2} = -x_{m3}$ while the critical coupling λ_{c2} is the same as in the t_1 case, i.e., $\lambda_{c2} = \lambda_{c3}$. It follows that $t_2 = t_1$. In fact, similar calculations also show that $t_1 = t_2 = t_3$.

To calculate t_4, we observe (see Fig. 2.21) that, on this interval, the dominant part of $x_3(t)$ increases from -1 to 0 while the element $x_1(t)$ remains in its steady state $x_- \approx -1$, so the behavior of x_3 is well approximated by

$$\dot{x_3}(t) = -x_3 + \tanh c(x_3 - \lambda + \varepsilon), \tag{2.36}$$

which yields

$$t_4 = \int_{-1}^{0} \frac{dx_3}{\tanh c(x_3 - \lambda + \varepsilon) - x_3}. \tag{2.37}$$

Once again, we can show that the critical coupling at which the local potential function $U(x_3)$ (dynamics restricted to the interval t_4) has an inflection point is given by

$$\lambda_{c33} = \varepsilon - x_{inf} + \frac{1}{c} \tanh^{-1} x_{inf}. \tag{2.38}$$

Direct calculations also show that the denominator of (2.37) is sharply peaked at $x_{m33} = \lambda - \lambda_{c33} - x_{inf}$. Then we expand this denominator about x_{m33} to get

$$\tanh c(x_3 - \lambda + \varepsilon) - x_3 \approx \lambda_{c33} - \lambda - cx_{inf}(x_3 - x_{m33})^2. \tag{2.39}$$

Using the relation $\lambda_{c33} = \lambda_{c3} + 2\varepsilon$, we finally arrive at an expression for t_4

$$t_4 \approx \int_{-\infty}^{\infty} \frac{dx_3}{\lambda_{c3} - \lambda + 2\varepsilon + cx_{inf}(x_3 + x_{m33})^2} = \frac{\pi}{\sqrt{cx_{inf}}\sqrt{\lambda_{c3} - \lambda + 2\varepsilon}}. \tag{2.40}$$

In addition, we can show that $t_4 = t_5 = t_6$. Thus we may now write down the oscillation periods, $T_i, i = 1, 2, 3$, of the individual waveforms in terms of t_1 and t_4.

After some algebra we find that $T_1 = 3(t_1+t_4)$ and the other two periods are identical, i.e., $T_1 = T_2 = T_3$. Using the integral approximations to t_1 and t_4, Eqs. (2.32) and (2.40), respectively, we arrive at

$$T_i = \frac{3\pi}{\sqrt{cx_{inf}}}\left[\frac{1}{\sqrt{\lambda_{c3}-\lambda}} + \frac{1}{\sqrt{\lambda_{c3}-\lambda+2\varepsilon}}\right]. \tag{2.41}$$

We note that this last equation is identical to the one that describes the period of the individual output signals of the standard configuration. However, as we will show next, the Residence Times Difference (RTD) for the AO configuration is different depending on the element under consideration, as readily apparent in Fig. 2.21. Using Fig. 2.21 as a reference, we may also write down the RTDs for all three waveforms in terms of t_1 and t_4. This leads to $\Delta_1 t = 3(t_1 - t_4)$ and $\Delta_2 t = \Delta_3 t = t_1 - t_4$, corresponding, respectively, to the signals $x_i(t)$ $(i = 1 - 3)$. Clearly, the waveform $x_1(t)$ is more sensitive (to small changes in the dc target signal) than the other two outputs by a factor of 3. From (2.32) and (2.40), respectively, we then obtain a closed-form expression for the RTD using x_1 as a detection signal:

$$\Delta_1 t = \frac{3\pi}{\sqrt{cx_{inf}}}\left[\frac{1}{\sqrt{\lambda_{c3}-\lambda}} - \frac{1}{\sqrt{\lambda_{c3}-\lambda+2\varepsilon}}\right]. \tag{2.42}$$

This last equation reveals that the sensitivity of $x_1(t)$ in the AO configuration is exactly three times the best sensitivity response that can be achieved by the standard configuration. We note that, in the latter case, the RTDs corresponding to all the output waveforms are identical and they are, moreover, identical to the RTD obtained via the summed output. The above-demonstrated improvement in the RTD for the AO case is even better for larger networks as we demonstrate next.

The generalization of the above observations to rings of arbitrary size N is straightforward. Similar computer simulations and calculations show that there are now N intervals of size t_1 and N intervals of size t_{N+1}. The period T_i, $i = 1, \ldots, N$, of the individual signals are all the same: $T_i = N(t_1 + T_{N+1})$. Using signal $x_1(t)$, the RTD is $\Delta_1 t = N(t_1 - t_{N+1})$. For the remaining signals the RTD is $\Delta_j t = t_1 - t_{N+1} = (1/N)\Delta_1$, $j = 2, \ldots, N$. Direct calculations of t_1 and T_{N+1} then lead to the following analytic results:

$$T_i = \frac{N\pi}{\sqrt{cx_{inf}}}\left[\frac{1}{\sqrt{\lambda_{c3}-\lambda}} + \frac{1}{\sqrt{\lambda_{c3}-\lambda+2\varepsilon}}\right], \tag{2.43}$$

and,

$$\Delta_1 t = \frac{N\pi}{\sqrt{cx_{inf}}}\left[\frac{1}{\sqrt{\lambda_{c3}-\lambda}} - \frac{1}{\sqrt{\lambda_{c3}-\lambda+2\varepsilon}}\right]. \tag{2.44}$$

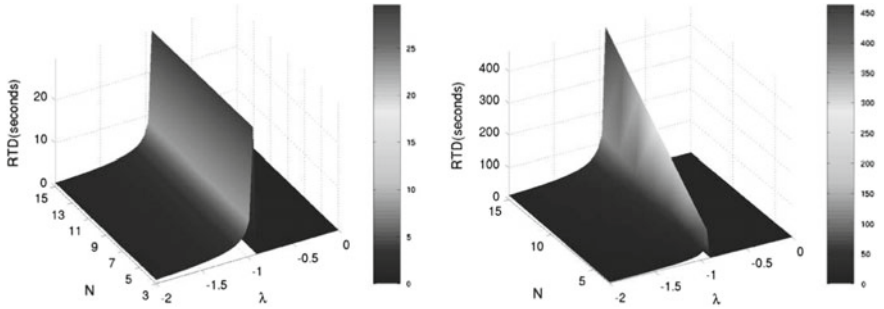

Fig. 2.22 RTD response of a CCFM as a function of ring size N and of coupling strength λ. *Left* standard configuration and *right* AO configuration. Near the onset of coupled-induced oscillations, in particular, the RTD response of the standard configuration remains constant (as expected) while that of the AO configuration increases linearly as as a function of N. $c = 3, \varepsilon = 0$

Recall that $\partial \Delta t / \partial \varepsilon$ measures the sensitivity of a CCFM (in the standard orientation). It follows that

$$\frac{\partial \Delta_1 t}{\partial \varepsilon} = N \frac{\partial \Delta t}{\partial \varepsilon}.$$

In other words, the sensitivity of the AO configuration, using $x_1(t)$ as the detecting signal, improves, linearly, by a factor of N when is compared to the best sensitivity that can be achieved by the summed output signal of the standard configuration, given the same external signal and core parameters. The dependence of the RTD, and consequently of the sensitivity, on the size of the ring in the AO configuration is in direct contrast to the sensitivity response of the standard configuration, in which increasing N beyond $N = 3$ does not lead to additional benefits. We should emphasize that the standard configuration, nevertheless, still outperforms the sensitivity of a magnetometer based on a single uncoupled core. The above observations are confirmed in Fig. 2.22, in which we calculate, numerically, the RTD $\Delta_1 t$ for a CCFM system with standard as well as with AO configuration.

As expected, near the onset of coupling-induced oscillations, the RTD response of the standard configuration remains constant while that of the AO configuration increases, linearly, as a function of N. The RTDs were calculated using the summed output signal $\Sigma x_i(t)$ for the standard configuration (as already mentioned, this RTD is identical to that obtained via individual elements for the standard configuration), and the individual signal $x_1(t)$ for the AO configuration.

It is clear that, for rings of arbitrary odd N elements, one always has a situation wherein two adjacent elements have the same orientation (i.e. the sign of the dc term in the dynamics (2.26) is the same for these two elements). In this case, the most sensitive (in the RTD) element is always the one (out of these two elements) which is forward coupled to an element with the opposite orientation. For example, in the system at hand, x_3 and x_1 have the same orientation, with x_3 forward coupled to x_1 (same orientation) but x_1 forward coupled to x_2 (opposite orientation); hence x_1 is

the most sensitive for detecting the target dc signal via the RTD. The effect of the AO configuration on the sensitivity seems to be universal for other sensor systems that are underpinned by unidirectionally coupled bistable element e.g., the behavior can be predicted theoretically, and verified via simulations in an electric field sensor [199] which is realized by unidirectionally coupling N ferroelectric core elements which, whilst being bistable, have potential energy functions quite different in structure to the ferromagnetic case treated here.

2.7 AC Field Detection

In this section, we explore the response of the coupled magnetometer system to a time-periodic magnetic flux signal, applied to each element in the array; effectively, we introduce another frequency (in addition to the network oscillation frequency in the absence of the signal) into the dynamics. The coupled system response, then, shows a richness of dynamical behaviors not seen in its single driven counterpart. We now describe this behavior, starting with the dynamics [195] for three unidirectionally (cyclically) coupled fluxgate magnetometers:

$$\tau \dot{x}_i = -x_i + \tanh(c(x_i + \lambda x_{i+1} + h(t))), \tag{2.45}$$

where τ is the device time constant, $x_i(t)$ represents the (suitably normalized) magnetic flux at the output (i.e. in the secondary coil) of unit i, $i = 1, 2, 3,\ \mathrm{mod}3$ and $h(t) = \varepsilon \sin \omega t$ is an externally applied "target" magnetic flux ($\varepsilon \ll U_0$), U_0 being the energy barrier height (absent the coupling) for each of the elements (assumed identical for theoretical purposes).

Numerically integrating the system (2.45), with non-identical initial conditions and $h(t) = \varepsilon \sin \omega t$, reveals three distinctive regimes of oscillatory behavior that are clearly separated (Fig. 2.25) in the parameter space (λ, ε): (I) The *supercritical* regime wherein the coupling parameter is below the critical value ($\lambda < \lambda_0$, i.e. $|\lambda| > |\lambda_0|$ in our convention). In this regime, the coupled system oscillates with a traveling wave pattern as described above, even for $h(t) = \varepsilon$, as long as the initial conditions for at least two of the elements are non-identical. In the presence of the target signal $h(t)$, the system responds by oscillating asymmetrically between the two stable magnetization states of each element. The response displays a frequency mixing of the inherent oscillations of the coupled system and the target signal. Poincaré sections computed from the phase space $(x_1(t), x_2(t), x_3(t))$, see Fig. 2.23, can help us identify the various qualitative states of the dynamics and the bifurcations that occur as the coupling strength in the network varies.

As λ varies, the phase-space solution $(x_1(t), x_2(t), x_3(t))$ exhibits a series of complex transitions to quasi-periodic motion and even chaotic motion. Figure 2.24 shows the bifurcation diagram in which we can visualize the complex transitions through the Poincare map dynamics.

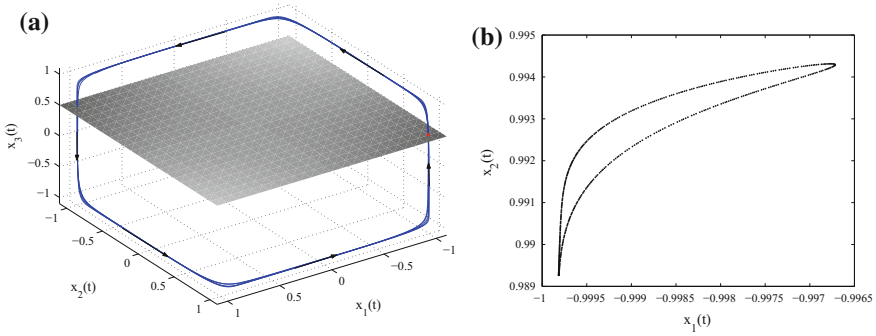

Fig. 2.23 **a** Poincaré map of the dynamics of a fluxgate network, employed for the detection of ac signals, computed from (2.45). **b** Solution projected onto the phase plane $(x_1(t), x_2(t))$. Parameters are: $c = 3$, $\lambda = -0.5$, $\varepsilon = 0.05$, and $\omega = 0.07$. *Arrows* indicate the direction of flow

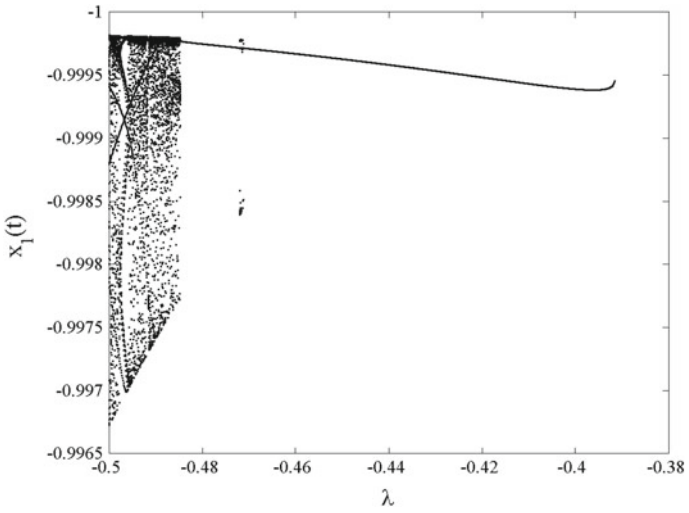

Fig. 2.24 Bifurcation diagram depicting complex transitions in the Poincaré map of a network of ac fluxgate sensors. The transitions occur as the coupling strength λ changes

(II) The *subcritical* regime wherein the coupling strength exceeds the critical value ($\lambda > \lambda_0$, $|\lambda| < |\lambda_0|$), so that there are no spontaneous oscillations. For small $h(t)$, the system oscillates about the steady states near ± 1. With sufficiently large $h(t)$, the system oscillates between the two steady states in a travelling wave pattern where the amplitude and frequency of each oscillation are the same but a phase shift of $\frac{2\pi}{3}$ exists between the different waveforms. This behavior is quite similar to that already observed for the case of dc (or zero) target signal; however, the onset of the oscillations occurs sooner in parameter space when the applied signal is time-periodic. The oscillation frequency is exactly $\omega/3$. (III) Frequency matching of the output waveform to that of the target signal. With the control parameter λ held

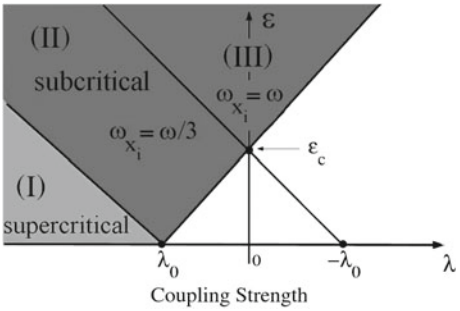

Fig. 2.25 Theoretical Phase Diagram: Oscillatory behavior of the coupled fluxgate model (2.45) in parameter space (λ, ε). In the supercritical regime, the oscillations form a traveling wave pattern. In the subcritical regime, with $h(t)$ small, the system oscillates about one of the steady states ± 1, while with $h(t)$ large, the system oscillates between two steady states. In both cases the oscillation form a travelling wave and their frequency is exactly $\omega/3$. For ε greater than a critical value, all three waves are in-phase with each other and frequency synchronized with the external signal $h(t)$ in region (III)

constant in the subcritical regime, increasing ε past a critical value causes the coupled system to switch to another oscillation mode wherein the frequency of the output waveform precisely match with that of the target signal. This behavior occurs solely in the presence of a time-periodic applied signal, within the parameter space bounded by the dashed lines in Fig. 2.25. For signal detection purposes, the subcritical regime is more relevant since it is relatively easy to extract information about the target signal, via the Residence Time Detection (RTD) method [60, 195], because of the simplicity of the oscillation characteristics e.g. constant amplitudes, frequencies, and phases; the RTD technique is not, however, as easy to use in the supercritical regime.

Let us consider the more interesting (from the weak signal detection standpoint) *sub*critical regime in this book. We begin with an analytic calculation of the critical coupling strengths for the onset of the oscillations as function of the target signal amplitude ε and frequency ω. These results afford us the capability to set the boundaries, in parameter space, of the different types of oscillation characteristics in the subcritical regime (Fig. 2.25).

For a given ω and moderate values of (λ, ε) above the boundary line for the supercritical regime, each element oscillates at $\frac{1}{3}\omega$, with an inter-element phase difference of $2\pi/3$. When the amplitude is large enough, the oscillations switch to an in-phase pattern with a frequency perfectly matched to the external signal frequency. This out-of-phase region is bounded (Fig. 2.25) by the *super*critical region (below) and the in-phase region (above). To the right, the region is bounded by the line connecting λ_0 and the critical signal amplitude ε_c where the entrainment between the uncoupled ($\lambda = 0$) system and the external signal occurs. So the critical coupling $\lambda_{c_{sub}}$ for the onset of the oscillations, which is described by the line, for a given ε is

$$\lambda_{c_{sub}} = \lambda_0 - \left(\frac{\lambda_0}{\varepsilon_c}\right)\varepsilon. \tag{2.46}$$

Our strategy for finding an analytical expression for $\lambda_{c_{sub}}$ rests, therefore, on the ability to compute the critical value ε_c. For this, we consider the uncoupled system with the reduced elemental dynamics

$$\tau\dot{x} = -x + \tanh(c(x + \varepsilon \sin \omega t)). \tag{2.47}$$

The change of variable $y = x + \varepsilon \sin(\omega t)$ with re-scaling and re-labeling time using $\omega t + \phi = \omega t + \cos^{-1}(1/\sqrt{1+\omega^2\tau^2})$, allows us to transform (2.47) into the more convenient form

$$\dot{y} = -y + \tanh(cy) + \tilde{\varepsilon} \sin(\omega t), \tag{2.48}$$

where $\tilde{\varepsilon} = \varepsilon\sqrt{1+\omega^2\tau^2}$. Next we approximate $-y + \tanh(cy)$ near $y = 1$, which is one of the equilibrium (magnetization steady state) points, with a second order polynomial $d + by + ay^2$, where a, b, and d are constant parameters that depend on the nonlinearity parameter c, and can be found via a Taylor expansion about $y = 1$:

$$\begin{aligned} a &= \tfrac{(4c^2-4c^2e^{2c})e^{2c}}{(e^{2c}+1)^3}, \\ b &= \tfrac{(-3+4c-8c^2)e^{2c}+(-3+4c+8c^2)e^{4c}-e^{6c}-1}{(e^{2c}+1)^3}, \\ d &= -(a+b) + \left(\tfrac{e^{2c}-1}{e^{2c}+1} - 1\right). \end{aligned} \tag{2.49}$$

We then seek an asymptotic solution of the form $y = y_0 + \tilde{\varepsilon} y_1 + \varnothing(\tilde{\varepsilon}^2)$, to the simplified dynamics $\dot{y} = d + by + ay^2 + \tilde{\varepsilon}\sin(\omega t)$. Substitution readily yields the system,

$$\dot{y_0} = d + by_0 + ay_0^2 \tag{2.50}$$

$$\dot{y_1} = (b + 2ay_0)y_1 + \sin(\omega t), \tag{2.51}$$

which we now solve. The unperturbed problem (2.50) is a Ricatti equation, which we solve using a three-steps standard approach. Step 1, search for a particular solution $y_0 = A(a, b, d)$. Direct substitution into (2.50) yields $A = (-b - \sqrt{b^2 - 4ad})/2a$, where $(b^2 - 4ad)$ must be non-negative. Step 2, use the change of variable $y_0 = A + u$ to transform the Ricatti equation into a Bernoulli equation in u, given by: $\dot{u} = (a + 2aA)u + au^2$. Step 3, transform the Bernoulli equation into a first order linear DE by substituting $w = 1/u$, which yields $\dot{w} = -a - (a+2aA)w$. This linear equation can be readily solved and then back substitution into u and, in turn, into y_0 leads to

$$y_0(t) = A + \frac{1}{C_1 e^{-(b+2aA)} - \frac{a}{(b+2aA)}}, \tag{2.52}$$

where $C_1 = \frac{a}{(b+2aA)} + \frac{1}{y_0(0)-A}$. Direct substitution of y_0 into (5.15) and using standard methods yields a complete solution for y_1 given by:

$$y_1(t) = \frac{C_2 e^{(b+2aA)t}}{(C_1 - \frac{a}{b+2aA} e^{(b+2aA)t})^2} - \frac{\sin(wt+\phi)}{\sqrt{(b+2aA)^2+\omega^2}}, \tag{2.53}$$

where $C_2 = y_1(0)(C_1 - a/(b+2aA))^2$. Combining (2.52) and (2.53) yields a complete solution, up to order $\varnothing(\tilde{\varepsilon}^2)$, of (2.48), whence it can be shown that the asymptotic behavior of the original variable x is

$$\lim_{t\to\infty} x(t) = A - \left(\frac{\sqrt{1+\omega^2\tau^2}}{\sqrt{(b+2aA)^2+\omega^2\tau^2}} + 1 \right) \varepsilon \sin(\omega t). \tag{2.54}$$

At the critical amplitude, ε_c, the nonzero-mean periodic solution $x(t)$ merges into a zero-mean periodic solution. This occurs when

$$\varepsilon_c = \frac{A\sqrt{(b+2aA)^2+\omega^2\tau^2}}{\sqrt{1+\omega^2\tau^2} + \sqrt{(b+2aA)^2+\omega^2\tau^2}}. \tag{2.55}$$

For the *super*critical case one can, analogous to (2.46), write down (see Fig. 2.25)

$$\lambda_{c_{sup}} = \lambda_0 + \left(\frac{\lambda_0}{\varepsilon_c} \right) \varepsilon, \tag{2.56}$$

2.8 Target Signal Contamination

We expect noise in our CCFM to arise from three sources: a magnetic noise floor (due to the core material and, in particular, magnetic domain motion), contamination of the target signal, and noise from the electronics in the coupling circuitry. In recent work we studied, numerically, the effects of an additive magnetic noise floor [59]. We now investigate the case of a target signal contaminated by noise, assumed to be Gaussian band-limited noise having zero mean, correlation time τ_c, and variance σ^2. This type of noise is a good approximation (except for a small $1/f$ component at very low frequencies) to what is actually observed in the experimental setup. From a modeling point of view, colored noise $\eta(t)$ that contaminates the signal should appear now as an additive term inside the tanh function of Eq. (2.6), i.e.,

$$\begin{aligned} \frac{dx_i}{dt} &= -x_i + \tanh(c(x_i + \lambda x_{i+1} + \varepsilon + \eta_i(t))) \\ \frac{d\eta_i}{dt} &= -\frac{\eta_i}{\tau_c} + \frac{\sqrt{2D}}{\tau_c}\xi(t). \end{aligned} \tag{2.57}$$

In general, we would expect somewhat different noise in each equation, since, realistically, the reading of the external signal ε is slightly different in each core. This is due to non-identical circuit elements and cores, mainly. In this work we will

consider, therefore, the situation wherein the different noise terms $\eta_i(t)$ are uncorrelated; however, for simplicity, we will assume them to have the same intensity D. Each (colored) noise $\eta_i(t)$ is characterized by $\langle \eta_i(t) \rangle = 0$ and $\langle \eta_i(t)\eta_i(s) \rangle = (D/\tau_c) \times \exp[-|t-s|/\tau_c]$, where $D = \sigma^2\tau_c^2/2$ is the noise intensity, and the "white" limit is obtained for vanishing τ_c; in practice, however, the noise is always band-limited. In this formulation, we assume the signal to be contaminated purely by external noise; in future work, however, we will also consider other sources of contamination such as internal noise introduced by each individual core, as well as the coupling and readout circuits.

We assume the temperature-related parameter c to be constant throughout our simulations and the target signal to be $\varepsilon = 0.07$, well below the energy threshold of a single (uncoupled) core. Of course, the results are expected to be similar to those found at other values of the target signal within the energy barrier height.

Figure 2.26 shows the relation between the mean oscillation frequency of (a single core element of) the CCFM with $N = 3$ cores and the system parameters (coupling strength λ and noise intensity D). The mnemonic "SO" in the figure stands for standard orientation, in which all the individual cores have the same spatial orientation (i.e. the sign of the target signal term is the same in each equation of the system (2.57)) for signal detection purposes. A sample of one thousand time-series simulations was then used to compute the frequency output at each point in parameter space $(\lambda,\ D)$. Each simulation was carried out with correlation time set to $\tau_c = 150$ since typically $\tau_F \ll \tau_c$, where $\tau_F = 1$ is the time constant of the core dynamics given by (2.6). Observe that the critical-coupling bifurcation point λ_c of the deterministic system, i.e., $D = 0$, remains, approximately, unchanged for small values of noise intensity. There is, however, a subtle shift in the bifurcation point for increasing noise (beyond

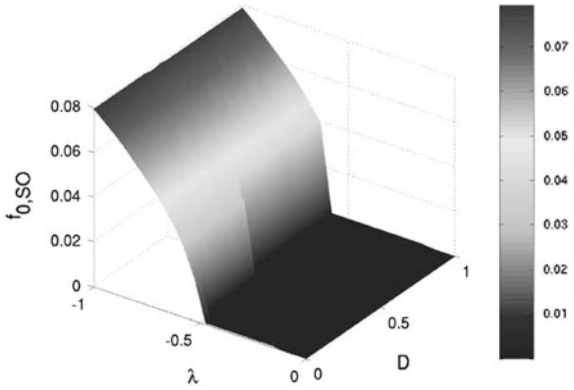

Fig. 2.26 Frequency (Hz) response of simulations of a CCFM system, subject to parametric noise, as a function of coupling strength λ and noise intensity D. Parameters are: $N = 3$ cores, $c = 3$, $\tau_c = 150$, and $\epsilon = 0.07$. SO denotes the standard orientation in which all individual fluxgates are similarly oriented for signal detection purposes. Observe that the onset of coupling-induced oscillations shifts slightly (to the left of λ_c) for larger values of noise intensity, as is shown by the small dent in the surface plot near $D = 0.5$

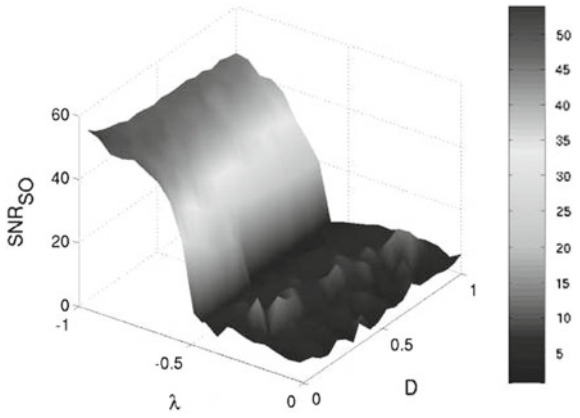

Fig. 2.27 Signal-to-Noise-Ratio output of (a single element) of a CCFM system in the presence of parametric noise. Parameters are: $N = 3$ cores, $c = 3$, $\tau_c = 150.0$, and $\epsilon = 0.07$

$D = 0.25$). The noise appears to have the effect of delaying the onset of oscillatory behavior. We find (not shown) that the delay is less pronounced in the more idealized scenario in which the noise $\eta_i(t)$ is taken to be the same in each core. Next we study the response of the CCFM through the Signal-to-Noise-Ratio (SNR). Figure 2.27 shows the SNR (of the output of a single core element) in the same parameter space (λ, D). The SNR increases rapidly near the critical coupling, as we would expect. The negative effects of highly contaminated signals (large noise intensity) appear to be well-mitigated by the sensitivity response of the system. To the right of the onset of oscillatory behavior, where the global dynamics of the deterministic system typically settle into a steady-state equilibrium, we now observe small fluctuations in the SNR caused mainly by noise. These fluctuations get smaller as the number of simulation samples increases.

It is worth mentioning that these small fluctuations are also present in the more ideal case wherein we take identical noise functions in each element of the dynamics. We now investigate the AO configuration which, as suggested by the results of the preceding section, as well as our laboratory experiments, holds out the promise of further performance enhancements. Finally, we study the effects of noise on the CCFM with the AO configuration. We use the output of the "favored" element that gives the best deterministic RTD response (see preceding section) in this configuration. Calculations of the SNR output of this "favored" element (not shown for brevity) show, at first glance, similar results to those of the standard-orientation configuration. A pointwise comparison between the SNR output of the two cases indicates, however, that the SNR output of (the favored element of) the AO configuration can be larger than that of the standard (CCFM) system (Fig. 2.28). Near the critical coupling strength, in particular, the SNR response of the AO system appears to be significantly better than that of the standard configuration. Large coupling strengths, on the contrary, reduce the SNR response of the AO configuration to values that are comparable to those of the standard case. The improvement in SNR output of the AO configuration over the standard (SO) case is also present in the ideal case of identical noises in the cores;

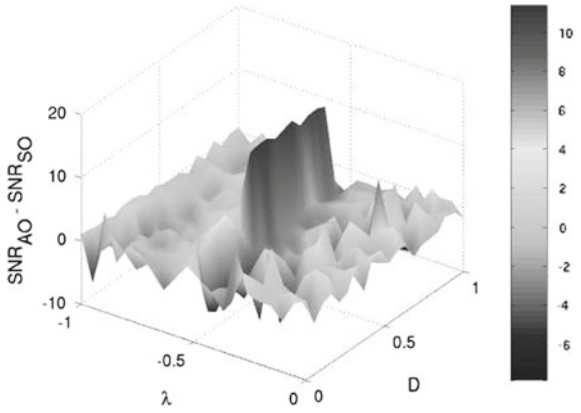

Fig. 2.28 Difference in SNR response between AO and SO configurations. Observe that near the onset of coupling-induced oscillations the SNR response of the AO configuration is significantly better. Parameters are: $N = 3$ cores, $c = 3$, $\tau_c = 150.0$ and $\epsilon = 0.07$

however, in this case, the improvement occurs for smaller values of noise intensity. In both cases, non-identical and identical noise terms, the difference between the SNR outputs suggests that careful tuning of the coupling strength can mitigate the negative effects of signal contamination so that full advantage can be taken of the sensitivity enhancements of a CCFM system with AO configuration.

2.9 Effects of Nonhomogeinities

In this section, we investigate the effects of nonhomogeneity in the thermal- and material-dependent parameter that controls the onset of oscillations of the network system. That parameter is proportional to the ratio of the Curie temperature T_c to the operating temperature T of the system. Imperfections due to processes or compositions in the ferromagnetic materials can, in principle, lead to variations in the temperature-dependent parameter of each individual sensor element, which could then affect the onset of oscillations of the entire network as well as its range of operation. We combine numerical simulations and analytical work to show that such nonhomogeneity can lead to a shift in the onset of oscillations in such a way that the network behaves as a homogeneous one with its onset of oscillation controlled by the single element with the largest nonlinearity parameter. In addition, we characterize the frequency response and compare it to that of the homogeneous case. The comparison shows that large variations in temperature parameters can render certain detection mechanisms, such as the Residence Times Detection technique, not applicable over the sum signal response due to the appearance of more than one frequency of oscillation in its time series. However, the computer simulations reveal that the statistical properties of the inhomogeneous network, in particular the probability distribution function of Residence Times Difference (RTD) readouts applied to individual signals, tend to those of a homogeneous network with (identical) c-values equal to the average of those of a nonhomogenous network.

While the use of homogeneous values for the temperature-related parameter c is a modeling assumption that facilitates a first attempt to study, theoretically, the underlying dynamics of the coupled system, it is, however, unlikely that such assumption would hold in an actual experimental implementation. Slight material imperfections within a ferromagnetic core can lead, for instance, to slight variations in the operating values of c. It is then more reasonable that we re-cast the original Eq. (2.6) into a more realistic model of the form

$$\dot{x}_i = -x_i + \tanh[c_i(x_i + \lambda x_{i+1} + \epsilon)], \tag{2.58}$$

where the subscript in c_i indicates the temperature-related parameter c for each individual element i.

Onset of Oscillations. Figure 2.29 shows a one-parameter bifurcation diagram for a nonhomogeneous network system (2.58) with $N = 3$. The diagram is similar to that of Fig. 2.7 except that now the branch of unstable equilibria that bifurcates off of the zero equilibrium $||X|| = 0$, where $X = (x_1, \ldots, x_N)$, undergoes a series of twists and turns before it reaches the branch of stable equilibria where $||X|| = 1$. Such twists are a direct result of the asymmetry introduced into the system by the heterogeneity of the c values. Each individual overdamped system is bistable while the coupled-system (2.58) is a multistable system with $2N$ equilibrium points. However, a critical observation is that there is only one branch of globally asymptotically stable oscillations, which is created from the collective behavior of the individual systems. Thus the same solutions, i.e., periodic oscillations, are obtained regardless of the initial conditions, as long as the coupling strength is set within the limits where the branch of oscillations exists.

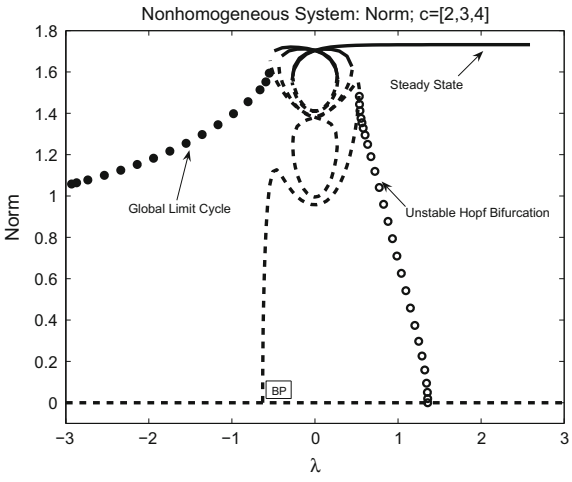

Fig. 2.29 One-parameter bifurcation diagram showing a branch of globally asymptotically stable periodic oscillations *(filled-in circles)* in the nonhomogeneous coupled fluxgate system (2.58) with $N = 3$ and $c_i = [2, 3, 4]$. A similar branch, including its stability properties, appears in larger arrays, as long as N is odd

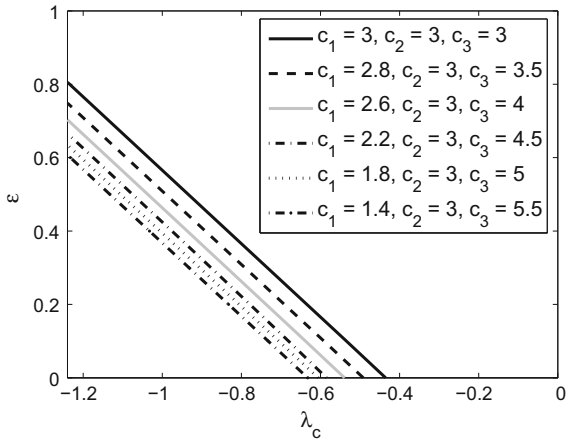

Fig. 2.30 Two-parameter bifurcation curves outlining the onset of oscillations in the nonhomogeneous coupled fluxgate system (2.58) for different combinations of the temperature-related parameter c. For any given curve, oscillations occur for values of (ε, λ) that are below that curve. On the other side of the curve the system settles quickly into a steady state. The curves shift to the left when at least one of the $c_{i's}$ increases

Another issue in the heterogeneous system is the location of the critical coupling strength λ_c. In fact, closer examination of Fig. 2.29 seems to indicate that the location of the critical coupling strength has shifted slightly to the left of that of the homogeneous case. Indeed, Fig. 2.30 confirms that the locus of the onset of oscillations, parameter space (ε, λ_c), moves leftward when at least one of the $c_{i's}$ increases. Effectively, the nonhomogeneous network behaves as a homogeneous one operating under the largest value of $c_{i's}$, i.e., $c = \max\{c_{i's}\}$.

We can explain, analytically, the numerically observed shift in λ_c by recalling from [195] that the coupling-induced oscillations in (2.57) emerge via an infinite-period bifurcation that limits in a heteroclinic cycle which connects the saddle equilibrium points of (2.57). At the birth of the cycle, solution trajectories are confined to the invariant stable/unstable manifolds (lines in phase space) of each of the saddles, which leads to the following conditions for the existence of a heteroclinic cycle

$$-x + \tanh(c_i(x - \lambda + \epsilon)) > 0 \tag{2.59}$$

$$-x + \tanh(c_i(x + \lambda + \epsilon)) < 0. \tag{2.60}$$

When $\varepsilon = 0$, the left-hand side of (2.59) is positive (for all values of $c_{i's}$) everywhere on the interval $[-1 : 1]$. Increasing ε only shifts the graphs vertically in the positive direction, so these conditions are always satisfied for all values of $c_{i's}$. When $\varepsilon = 0$, the left-hand side of (2.60) is negative everywhere on the interval $[-1 : 1]$ with a local maximum that approaches zero as λ approaches the bifurcation point λ_c. That local maximum is even larger for larger values of c, which explains why the

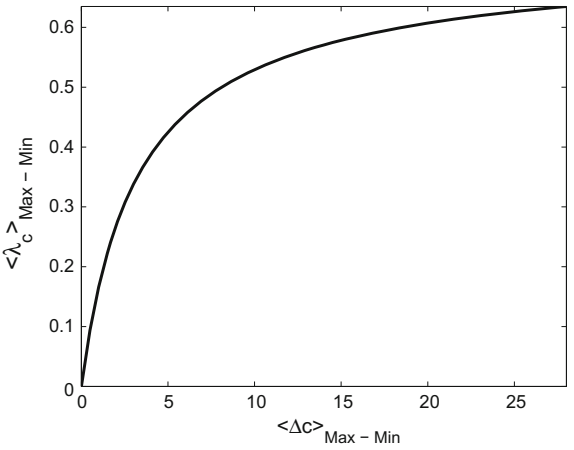

Fig. 2.31 Displacement in the critical coupling strength that is required for inducing oscillatory behavior in a network of nonidentical fluxgate sensors, coupled unidirectionally, as a function of the separation of the temperature-related parameters $c_{i's}$ between their maximum and minimum values (Δc). The *brackets* $<>$ denotes the average value

network dynamics is now driven by the largest of the $c_{i's}$. Note that direct calculations of that local maximum lead us to the analytical expression for λ_c, which is shown in Eq. (2.18).

In Fig. 2.31 we quantify the change in the critical coupling strength $\Delta\lambda_c$ as a function of the average separation between the highest and lowest value of the c_i values, Δc; Δc is measured by taking the average of $(\max\{c_i\} - \min\{c_i\})$ for an ensemble of different values of the temperature-related parameter c over the same type of configuration, i.e., unidirectionally coupled ring. Thus, when $\Delta c = 0$, the critical coupling λ_c associated with the highest and lowest values of c, respectively, are the same, so the average of their difference is 0. In other words, $\Delta\lambda_c = 0$. From Fig. 2.30 we notice that, although the highest $c$value is increasing at constant increments of 0.5, the corresponding two-parameter bifurcation curves are not being shifted leftward at constant increments. In fact, there is a visible decrease in the leftward movement of the two-parameter bifurcation curves as c increases. The natural question then becomes, is there a limit to the leftward shift in the two-parameter bifurcation curves? Though it appears that primarily it is the largest c-value that is driving the dynamics of the system, we still must take into account the contribution to the dynamics from the other individual units with lower c-values. In particular, we want to quantify the effect of the spread in the c-values on the critical coupling λ_c as a function of the average of the highest c_i minus the lowest c_i. The result is shown in Fig. 2.31. Observe that as Δc increases, $\Delta\lambda_c$ increases uniformly while it approaches, asymptotically, a limiting value, We can determine an analytical expression for that limiting coupling strength by taking the limit when $\varepsilon \to \infty$ on Eq. (10.49) and get: $\lambda_c^* = \lim_{c\to\infty} \lambda_c = -\varepsilon - 1$. The limiting critical coupling strength shown in Fig. 2.31 coincides very well with the theoretical limit. Furthermore, the theoretical result implies that in practical applications there is a point of diminishing return, where increasing the value of c (in any element, but specifically in the element with the highest c) will not yield a lower onset of oscillation point.

Frequency Response. Direct calculations similar to those of the homogeneous case yield the following expression for the period T of each individual element

$$T = \sum_{i=1}^{3} \frac{\pi}{\sqrt{c_i x_{inf_i}}} \left(\frac{1}{\sqrt{\lambda_{c_i} - \lambda}} + \frac{1}{\sqrt{\lambda_{c_i} - \lambda + 2\varepsilon}} \right). \tag{2.61}$$

The generalization of the above observations to rings of arbitrary size N is straightforward. Similar computer simulations and calculations show that there are now N intervals of size $t_1, \ldots, t_N$, in which the individual signals decrease from 1 to 0 while the elements to which they are coupled remain (approximately) in their steady state $x_+ \approx 1$. Likewise, there are also N intervals through which the individual signals increase from -1 to 0 while the elements to which they are coupled remain (approximately) in their steady state $x_- \approx -1$. Direct calculations show that the period T_N of the individual signals are all the same and is given by

$$T_N = \sum_{i=1}^{N} \frac{\pi}{\sqrt{c_i x_{inf_i}}} \left(\frac{1}{\sqrt{\lambda_{c_i} - \lambda}} + \frac{1}{\sqrt{\lambda_{c_i} - \lambda + 2\varepsilon}} \right). \tag{2.62}$$

We emphasize that as the $c_{i's}$ tend to an identical value, Eq. (2.62) reduces to that of the homogeneous case.

Sensitivity Response. In our previous work [195], the summed output signal $X(t) = \Sigma x_i(t)$ exhibited ideal characteristics for it to be the signal detector of the network: an almost sinusoidal signal with a single frequency. This is no longer the case in a nonhomogeneous network. As Fig. 2.32 shows it, the asymmetry introduced by the variations in c-values leads to a sum signal response with at least two distinct frequencies of oscillation. More specifically, the parameters that define the frequencies of the spectrum of the sum signal are: the temperature-related parameters c_i, the critical coupling strength λ_{c_i}, and the target signal ε. We note that the difference in the c values need not be large for the modulations to appear. In fact, small variations already lead to visible modulations in amplitude (frequency). The modulations are small but become more pronounced as the difference in c values get larger.

Consequently, signal detection via the RTD technique on the sum signal might not be readily feasible. Alternatively, we could implement the RTD readout using individual signals. Since they all share the same period, the difference in zero-crossing times Δt (which is a direct marker of the target signal ε) for a unidirectionally-coupled array, with $c_1 \leq c_2 \ldots \leq c_N$, then Δt_i, $i = 1, \ldots, N$, can be calculated by summing the intervals t_j, $j = (2i - 1), \ldots, N + 2i - 1 \bmod 2N$, in the upper states and t_j, $j = (N + 2i - 1), \ldots, 2N + 2i - 1 \bmod 2N$, in the lower state. Next by taking the difference of the upper and lower state we get the following expression where $a_{ij} = (-1)^{(j-i) \bmod N}$.

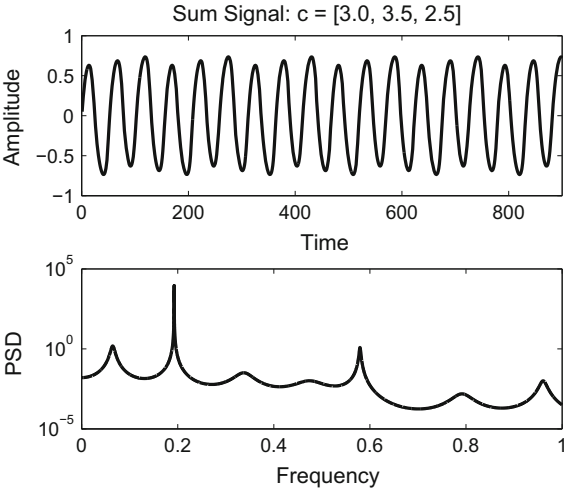

Fig. 2.32 (*Top*) Sum signal from simulations of a network of three nonhomogeneous bistable elements coupled in a directed ring. (*Bottom*) PSD decomposition of the sum signal shows the presence of more than one individual frequency of oscillation induced by the heterogeneity of the parameters: c_i, the critical coupling strength λ_{c_i}, and the target signal ε. Parameters are: $c_1 = 3$, $c_2 = 3.5$, $c_3 = 2.5$, and $\varepsilon = 0.0$

$$\Delta t_i = \left| \sum_{j=1}^{N} \frac{a_{ij}\pi}{\sqrt{c_j x_{inf_j}}} \left(\frac{1}{\sqrt{\lambda_{c_j} - \lambda}} - \frac{1}{\sqrt{\lambda_{c_j} - \lambda + 2\varepsilon}} \right) \right| \tag{2.63}$$

Figure 2.33 shows a good agreement between the RTD response to an applied target signal ε calculated analytically through Eq. (2.63) and numerically from simulations of the governing Eq. (2.58). For each individual value of the target signal the coupling strength λ is set to a value that is at a constant distance from the critical coupling strength λ_c, so that the device is always operating near criticality. For comparison purposes, the RTD response of a nonhomogeneous network is shown together with that of two closely related homogeneous networks. The homogeneous network with the smallest c value yields the best response; though, the improvement is marginal compared to the other networks.

We should note that a different ordering of non-identical c parameters may yield different RTD responses. Furthermore, the values of c are material-dependent, and can be difficult to measure precisely. Thus, in practice, it may not be feasible to speak of which arrangement will yield the best RTD. Instead, we would need to consider the statistical distribution of RTD responses for an ensemble of nonhomogeneous networks with variations in the c parameter. Computer simulations of such networks, with the values of c uniformly distributed between 1 and 5 with mean $\bar{c} = 3$, show that the Probability Distribution Function of RTD responses can be approximated by a Gaussian distribution of the form

$$P(RTD, \mu, \sigma) = \frac{31}{\sigma\sqrt{2\pi}} \exp\left(-\frac{(RTD - \mu)^2}{2\sigma^2} \right), \tag{2.64}$$

with mean $\mu = 0.54019656$ equal to the RTD of a homogeneous network with $c_i = \bar{c}$, for $i = 1, \ldots, N$, and standard deviation $\sigma = 0.1877035$.

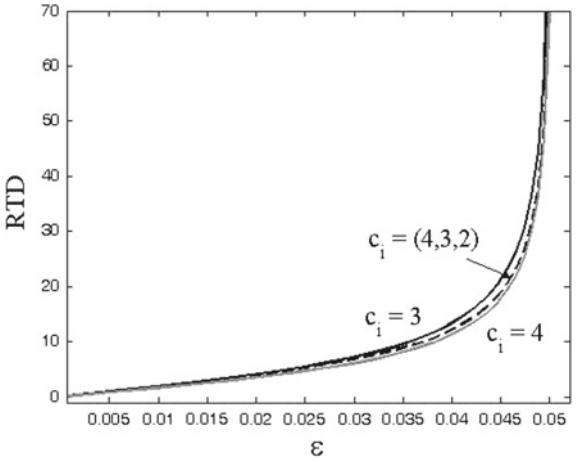

Fig. 2.33 RTD response to a target signal ε for a non-homogeneous coupled fluxgate system is compared to that of two closely-related homogeneous systems. *Solid lines* correspond to analytical calculations while individual markers are associated with numerical computations. All three networks, homogeneous and nonhomogeneous, operate near the critical coupling strength λ_c. That is, for each individual value of target signal ε the coupling strength λ is adjusted to a constant distance from the corresponding critical coupling strength λ_c as is shown in Fig. 2.30

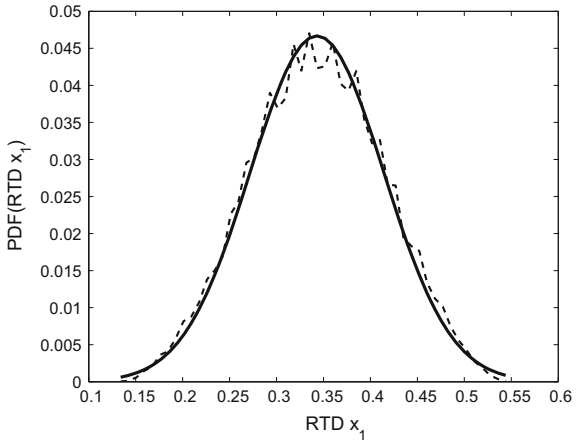

Fig. 2.34 Probability Distribution Function (PDF) of RTD response (measured for the x_1 element) to a target signal $\varepsilon = 0.07$ for a non-homogeneous coupled fluxgate system calculated numerically (*light line*) through an ensemble of about 100,000 sets of c values uniformly distributed between 1 and 5 with mean $\bar{c} = 3$. *Solid line* represents an analytical fitting which indicates that the PDF of RTD responses can be approximated by a Gaussian distribution with mean μ equal to the RTD of a homogeneous network with $c_i = \bar{c}$, for $i = 1, \ldots, N$

Figure 2.34 illustrates the actual fitting of (2.64) to the numerical estimate of the PDF(RTD) for the ensemble data. Additional simulations reveal that the statistical properties of the inhomogeneous network, in particular the probability distribution function of RTD readouts calculated using individual signals, tend to those of a homogeneous network with (identical) c-values equal to the average of those of a nonhomogenous network. As expected, shortening the width of the uniform distribution of c values, leads to a concommitant decrease in the standard deviation of $P(RTD)$.

2.10 Effects of Delay

While the mathematical models and related devices governed by bistable potential functions may assume instantaneous coupling, in practice we must account for the fact that even high-speed, high-precision, circuit components can introduce a delay in the coupling signal. Thus, in this section we investigate the behavior of a ring of overdamped bistable systems with delayed nearest-neighbor connections. We concentrate on the CCFM system as the "test-bed" to study the effects of time delay in generic formulations of coupled bistable systems. In this system, we have already shown that, without delay, large-amplitude oscillations and nontrivial synchronous equilibria can coexist near the onset of the oscillations. Our study shows that delay-induced Hopf bifurcation occurs from the synchronous equilibria but, generically, the small amplitude oscillations that appear are unstable. Thus, delay has the effect of decreasing the size of the basin of attraction of nontrivial synchronous equilibria, which in turn, makes the basin of attraction of the stable large-amplitude oscillations larger. Collectively, this is a positive effect because the sensor device depends mainly on large amplitude oscillations, so a small delay can make it easier to induce the device to oscillate on its own. As a "test bed", we use the model equations of a CCFM device with N fluxgates [267]. The results are, however, generic and applicable to all rings of overdamped bistable units unidirectionally coupled. For $N = 3$ the model equations are

$$\begin{aligned} \dot{x}_1(t) &= -x_1(t) + \tanh\left(c(x_1(t) + \lambda x_2(t-\tau_1) + \varepsilon)\right), \\ \dot{x}_2(t) &= -x_2(t) + \tanh\left(c(x_2(t) + \lambda x_3(t-\tau_2) + \varepsilon)\right), \\ \dot{x}_3(t) &= -x_3(t) + \tanh\left(c(x_3(t) + \lambda x_1(t-\tau_3) + \varepsilon)\right), \end{aligned} \tag{2.65}$$

where τ_1, τ_2, and τ_3, denote the corresponding delays in the connectivity scheme. Recall that we are primarily interested in the case where $\lambda < 0$, which is a negative feedback system.

The surface shown in Fig. 2.35 depicts the boundary between the basin of attraction of the synchronous equilibria and the large amplitude periodic oscillations. Initial conditions inside the pyramid-like shape are attracted to equilibrium points, while those outside are attracted to the large-amplitude oscillations. Observe that the size

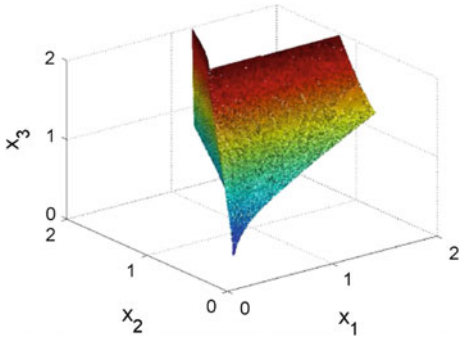

Fig. 2.35 Three dimensional surface defining the boundary between the basins of attraction of equilibrium points and that of periodic oscillations for a coupled-core fluxgate magnetometer, see Eq. (2.65), with $\tau = 0$. Points inside the pyramid-like shape are attracted to synchronous equilibria while those outside are attracted to a global branch of large-amplitude periodic oscillations. Parameters are: $c = 3$, $\lambda = -0.44$, $N = 3$, $\varepsilon = 0.0$

of the basin of attraction of the stable (nontrivial synchronous) equilibrium point gets larger as initial conditions move away from the origin.

We now return our attention to Eq. (2.65). We make the following change of variables to create a single delayed term with $\tau = \tau_1 + \tau_2 + \tau_3$

$$y_1(t) = x_1(t), \qquad y_2(t) = x_2(t - \tau_1), \qquad y_3(t) = x_3(t - (\tau_1 + \tau_2)).$$

The resulting system of equations is given by

$$\begin{aligned}
\dot{y}_1(t) &= -y_1(t) + \tanh\left(c(y_1(t) + \lambda y_2(t) + \varepsilon)\right), \\
\dot{y}_2(t) &= -y_2(t) + \tanh\left(c(y_2(t) + \lambda y_3(t) + \varepsilon)\right), \\
\dot{y}_3(t) &= -y_3(t) + \tanh\left(c(y_3(t) + \lambda y_1(t - \tau) + \varepsilon)\right),
\end{aligned}$$

where time is shifted for the second and third equations. For convenience (and greater generality), we consider the system given by:

$$\begin{aligned}
\dot{y}_1(t) &= -y_1(t) + f_1(y_1(t), y_2(t)), \\
\dot{y}_2(t) &= -y_2(t) + f_2(y_2(t), y_3(t)), \\
\dot{y}_3(t) &= -y_3(t) + f_3(y_1(t - \tau), y_3(t)),
\end{aligned} \tag{2.66}$$

where $f_1(y_1(t), y_2(t)) = \tanh\left(c(y_1(t) + \lambda y_2(t) + \varepsilon)\right)$, etc. We now wish to investigate the stability properties of the *synchronous* equilibria of the transformed system (2.66), see Fig. 2.7, which we denote by $(\bar{y}_1, \bar{y}_2, \bar{y}_3)$. The linearization of the above system is given by:

$$\begin{pmatrix} \dot{y}_1(t) \\ \dot{y}_2(t) \\ \dot{y}_3(t) \end{pmatrix} = \begin{pmatrix} -1+a_{11} & a_{12} & 0 \\ 0 & -1+a_{22} & a_{23} \\ 0 & 0 & -1+a_{33} \end{pmatrix} \begin{pmatrix} y_1(t) \\ y_2(t) \\ y_3(t) \end{pmatrix} + \begin{pmatrix} 0 & 0 & 0 \\ 0 & 0 & 0 \\ a_{31} & 0 & 0 \end{pmatrix} \begin{pmatrix} y_1(t-\tau) \\ y_2(t-\tau) \\ y_3(t-\tau) \end{pmatrix},$$

where

$$a_{11} = \frac{\partial f_1(\bar{y}_1, \bar{y}_2)}{\partial y_1}, \quad a_{12} = \frac{\partial f_1(\bar{y}_1, \bar{y}_2)}{\partial y_2}, \quad a_{22} = \frac{\partial f_2(\bar{y}_2, \bar{y}_3)}{\partial y_2},$$

$$a_{23} = \frac{\partial f_2(\bar{y}_2, \bar{y}_3)}{\partial y_3}, \quad a_{31} = \frac{\partial f_3(\bar{y}_1, \bar{y}_3)}{\partial y_1}, \quad a_{33} = \frac{\partial f_3(\bar{y}_1, \bar{y}_3)}{\partial y_3}.$$

Because we are primarily interested in the negative feedback system, $\partial f_i / \partial x_j < 0$ for $i \neq j$. As usual, we attempt to find solutions of the form $\mathbf{y}(t) = \boldsymbol{\xi} e^{\sigma t}$, with $\mathbf{y} = (y_1, y_2, y_3)^T$. It is not difficult to see that the resulting characteristic equation has the form:

$$\det \begin{bmatrix} -1+a_{11}-\sigma & a_{12} & 0 \\ 0 & -1+a_{22}-\sigma & a_{23} \\ a_{31}e^{-\sigma\tau} & 0 & -1+a_{33}-\sigma \end{bmatrix} = 0,$$

which is easily solved by expanding the first column to give:

$$(\sigma + 1 - a_{11})(\sigma + 1 - a_{22})(\sigma + 1 - a_{33}) - a_{12}a_{23}a_{31}e^{-\sigma\tau} = 0.$$

We are particularly interested in nontrivial *synchronous* equilibria of the form $(\bar{y}_1, \bar{y}_2, \bar{y}_3) = (\bar{y}, \bar{y}, \bar{y})$ so that $a_{11} = a_{22} = a_{33}$ and $a_{12} = a_{23} = a_{31}$. Note from Fig. 2.7 that there are exactly two nontrivial synchronous equilibria $(\bar{y}, \bar{y}, \bar{y})$ and $(-\bar{y}, -\bar{y}, -\bar{y})$. In both cases the characteristic polynomial reduces to:

$$(\sigma - A)^3 = B^3 e^{-\sigma\tau}, \tag{2.67}$$

where $A = a_{11} - 1$ and $B = a_{12}$. Direct calculations show that $0 < a_{11} < 1$ and $-1 < a_{12} < 0$, so that $-1 < A < 0$ and $-1 < B < 0$. We are interested in stability changes of the synchronous equilibria that may lead to small amplitude oscillations via a Hopf bifurcation. Those changes can only occur when $\sigma = \omega i$, and since the left-hand side of (2.67) is a polynomial function, monotonically increasing in magnitude and angle, then by the Argument principle of complex analysis Eq. (2.67) has a solution whenever $B < A$. To visualize this result, we can also solve (2.67) graphically, first substituting $\sigma = \omega i$ to obtain:

$$\left(\frac{A^3 - 3A\omega^2}{B^3}\right) + \left(\frac{\omega^3 - 3A^2\omega}{B^3}\right) i = -e^{-\omega\tau i}. \tag{2.68}$$

The left-hand side of (2.68) represents a complex-valued curve $\mathcal{C}_3(\omega)$ parametrized by ω while the right-hand side describes the unit circle in the complex plane, parametrized also by ω and by the delay τ. For $\tau > 0$, as ω increases (starting at zero) the right-hand term traces the unit circle S^1 clockwise starting at the point $(-1, 0)$, as is shown in Fig. 2.36(left).

Simultaneously, the left-hand curve $\mathcal{C}_3(\omega)$ traverses the complex plane counterclockwise starting at the point $(A^3/B^3, 0)$. When $B < A$ this starting point is in the interval $(0 < A^3/B^3 < 1, 0)$, and since the magnitude and angle of points traversed along $\mathcal{C}_3$ are monotonically increasing, then there is a critical value ω^* at which both the circle S^1 and $\mathcal{C}_3$ intersect. At $\omega = \omega^*$, the point of intersection on S^1 corresponds to a critical angle θ_c measured from the starting point $(-1, 0)$. The critical delay τ_c producing the Hopf bifurcation satisfies $\tau_c = \theta_c/\omega^*$. This critical delay corresponds to the solution of (2.68) at the Hopf bifurcation. By the periodicity of $e^{i\omega\tau}$, there are infinitly many solutions of (2.68), but other solutions produce larger values of τ, which are unstable. Analytically, ω^* is the solution of

$$\omega^6 + 3A^2\omega^4 + 3A^4\omega^2 + A^6 - B^6 = 0.$$

When $B = A$, see Fig. 2.36(middle), the point $(A^3/B^3, 0)$ has moved to $(1, 0)$ but the right-hand side term is still at $(-1, 0)$, so as soon as ω increases the point $(A^3/B^3, 0)$ separates away from the circle due to the monotonic nature of $\mathcal{C}_3$, thus there is no solution. Similarly, when $B > A$, Fig. 2.36(right), the starting point $(A^3/B^3, 0)$ is already separated from the unit circle and so there is no solution either.

The locus of the delayed-induced Hopf bifurcation points ω^*, in parameter space (λ, τ), is shown in Fig. 2.37a. The rightmost point along this two-parameter boundary curve corresponds to the condition $A = B$. The leftmost point is the Hopf bifurcation point without delay, i.e., $\tau = 0$. Substituting $\tau = 0$ in (2.68) we can solve for ω, which then yields the condition $B = 2A$ for the Hopf bifurcation without delay. Computational work conducted with the aid of DDE-BIFTOOL [110], a software tool for the bifurcation analysis of delay differential equations, confirms that the delay-

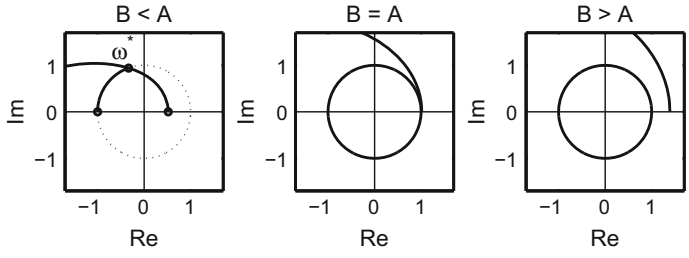

Fig. 2.36 Graphical representation of the solution set of Eq. (2.68)

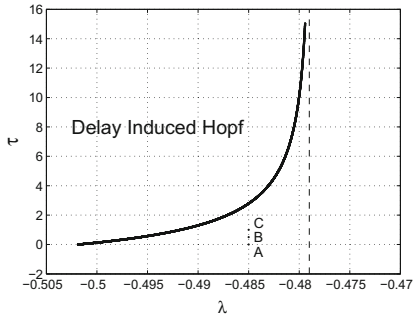

(a) Locus of delayed-induced Hopf

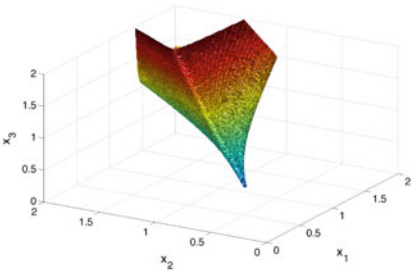

(b) A: $\tau = 0.0$

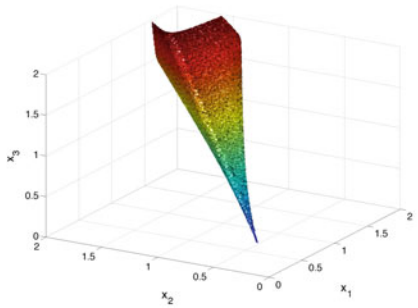

(c) B: $\tau = 0.5$

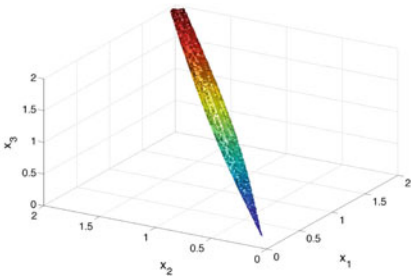

(d) C: $\tau = 1.0$

Fig. 2.37 **a** Locus of Hopf bifurcation induced by delayed coupling in a ring with $N = 3$ overdamped bistable systems governed by Eq. (2.69). **b–d** Basins of attraction of synchronous equilibria for delay values labeled A, B, and C in **a**, respectively. For small τ, both synchronous equilibria and large-amplitude oscillations have reasonably large basins of attraction. As τ increases towards the locus of the Hopf bifurcation, however, the equilibria lose stability, and consequently, their basins of attraction shrink accordingly

induced oscillations exist in the region just above the locus curve. The oscillations are, however, unstable. Figure 2.37b–d illustrate the contraction that occurs in the basin of attraction of synchronous equilibria due to delay-induced instability.

Generalization to Larger Arrays. We now consider the general case of N (odd) fluxgates governed by an N-dimensional system of coupled overdamped bistable units subject to delay:

$$\dot{x}_i(t) = -x_i(t) + \tanh\left(c(x_i(t) + \lambda x_{i+1}(t - \tau_i) + \varepsilon)\right), \tag{2.69}$$

where $i = 1, 2, \ldots, N \mod N$. We perform a similar change of variables to create a single delay term with $\tau = \tau_1 + \cdots + \tau_N$:

$$y_1(t) = x_1(t), \quad y_2(t) = x_2(t - \tau_1), \ldots, y_N(t) = x_N(t - (\tau_1 + \cdots + \tau_{N_1})).$$

The resulting system of equations is given by

$$\begin{aligned}\dot{y}_1(t) &= -y_1(t) + f_1(y_1(t), y_2(t)),\\ \dot{y}_2(t) &= -y_2(t) + f_2(y_2(t), y_3(t)),\\ &\vdots\\ \dot{y}_N(t) &= -y_N(t) + f_N(y_1(t-\tau), y_N(t)),\end{aligned} \tag{2.70}$$

where $f_1(y_1(t), y_2(t)) = \tanh\left(c(y_1(t) + \lambda y_2(t) + \varepsilon)\right)$, etc. The linearization of (2.70) with respect to the synchronous equilibrium solution $(y_1, \ldots, y_N) = (\bar{y}, \ldots, \bar{y})$, has the form

$$L = \begin{bmatrix} A & B & 0 & \ldots 0\\ 0 & A & B & \ldots 0\\ \vdots & & & \\ Be^{-z\tau} & 0 & 0 & \ldots A \end{bmatrix},$$

where $A = \partial f_i(\bar{y}, \bar{y})/\partial y_i - 1$ and $B = \partial f_i(\bar{y}, \bar{y})/\partial y_j$, $j \neq i$. Again we are most interested in the negative feedback system where $\partial f_i/\partial x_j < 0$ for $i \neq j$ and N is odd. The characteristic polynomial becomes $(\sigma - A)^N = B^N e^{-\sigma\tau}$, where σ represents again the eigenvalues of the linearized matrix L. Substituting the Hopf bifurcation condition $\sigma = \omega i$, we get

$$\frac{(A - \omega i)^N}{B^N} = -e^{-\omega\tau i}. \tag{2.71}$$

The left-hand side of (2.71) defines again a curve $\mathcal{C}_N(\omega)$ that traverses the complex plane counter-clockwise as ω increases from zero. This curve is similar to that of the $N = 3$ case, with $-1 < A < 0$ and $-1 < B < 0$, except that now the starting point is $(A^N/B^N, 0)$. When $B < A$, this starting point is in the interval $(0 < A^N/B^N < 1, 0)$ and so there is a critical value ω^* at which $\mathcal{C}_N$ intersects the unit circle at θ_c, i.e., the right-hand side of (2.71), so that the critical delay producing the Hopf bifurcation is once again $\tau_c = \theta_c/w^*$. The critical value ω^* can be found analytically by noticing that both sides of (2.71) are complex-valued expressions, which are equal only when their magnitudes and angles are identical, this produces the polynomial

$$(w^2 + A^2)^N = B^{2N},$$

whose solution ω^* yields the desired eigenvalue for the delayed-induced Hopf bifurcation point. Once again, the solution vanishes when the point $(A^N/B^N, 0)$ is at the opposite end point $(1, 0)$, which yields the condition $B = A$. Delayed-induced oscillations terminate at a regular Hopf bifurcation from the synchronous equilibrium with $\tau = 0$. To find this bifurcation point we note that when $\tau = 0$ the linearized matrix L becomes cyclic, with the eigenvectors space spanned by

$$V_j = \left\{\left[v, \zeta^j v, \zeta^{2j} v, \ldots, \zeta^{(N-1)j} v\right] : v \in R\right\},$$

where $\zeta = e^{2\pi/N}$. Direct calculations yield $L \cdot V_j = (A + \zeta^j B)V_j$. Hence the eigenvalues of $L|V_j$ are those of $A + \zeta^j B = A + \cos(2\pi j/N) + Bi \sin(2\pi j/N)$. It follows that a Hopf bifurcation occurs when

$$B = -\frac{1}{\cos(2\pi/N)} A. \tag{2.72}$$

Notice that this expression yields the previously found condition $B = 2A$ for the special case when $N = 3$. Figure 2.38 shows the locus, in parameter space (λ, τ), of the delayed-induced Hopf bifurcation point for $N = 5$ and $N = 7$, respectively. AUTO and numerical studies suggest that the delay-induced Hopf bifurcation is unstable leading to almost all solutions beyond the Hopf point approaching the large amplitude periodic orbit, making it a global attractor. However, we have not performed rigorous center manifold analysis [66] to prove instability of the Hopf bifurcation.

In each of these two cases, i.e., $N = 5$ and $N = 7$, small amplitude oscillations are found above the loci curves. A stability analysis conducted with the aid of DDE-BIFTOOL shows the small-amplitude, delay-induced, oscillations to be unstable. But this is good news for the coupled-core fluxgate magnetometer because the net effect of the delay is essentially to increase the basin of attraction of the global branch of large-amplitude oscillations between the two magnetization states of the ferromagentic materials. In other words, delayed coupling tends to enhance the basin of attraction of the global branch of oscillations so that it becomes more robust to induce a CCFM-based device to oscillate on its own.

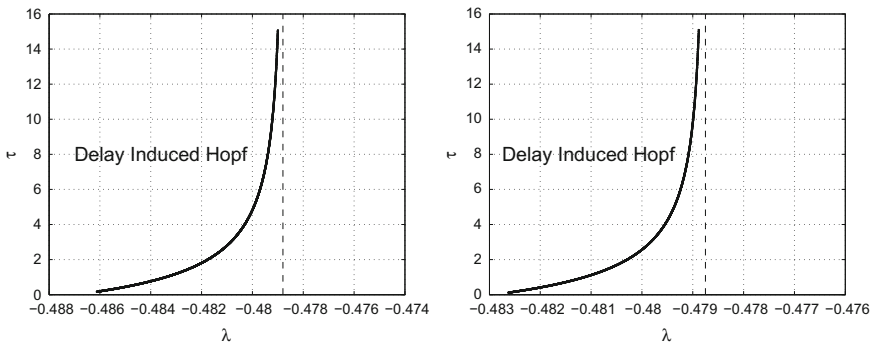

Fig. 2.38 Locus of Hopf bifurcation induced by delayed coupling in a ring with *left* $N = 5$ and *right* $N = 7$ overdamped bistable systems governed by Eq. (2.69)

2.11 Laboratory Implementation

The experimental coupled device involves three ferromagnetic cores together with the coupling circuit; the setup conforms to the model equation (2.6); in recent experiments, we have implemented the AO arrangement (2.26) which affords the prospect of enhanced sensitivity. Figure 2.39 shows the block diagram, as an overview, of the setup. The cores are not unique to this particular setup i.e., the same core design has been used in previous work involving only a single device. What is unique is the coupling circuitry that makes the coupled core devices realizable and have behaviors in accordance to the results of the preceding section. We now provide some details of the construction of the sensor and the coupling circuit.

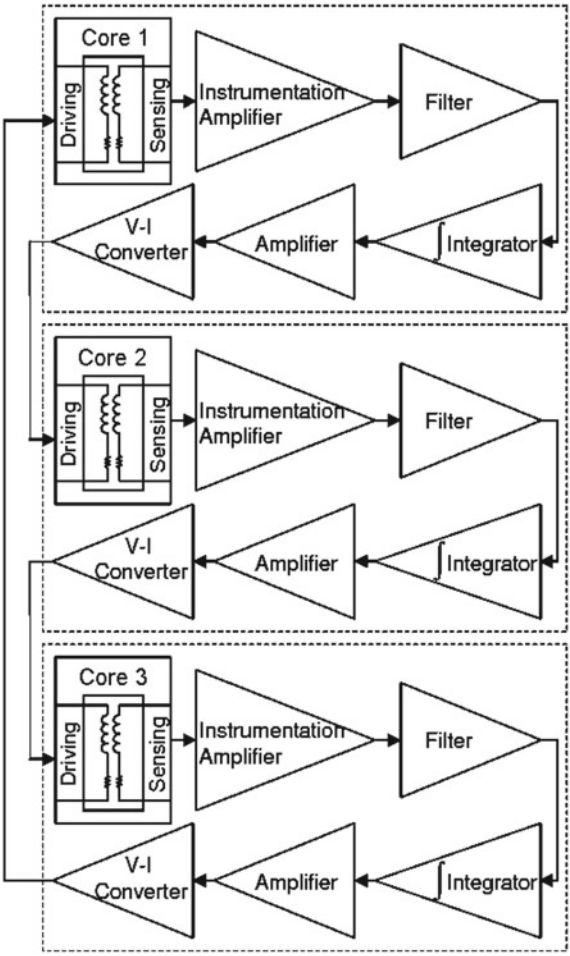

Fig. 2.39 Flow diagram of the $N = 3$ coupled core system as an overview for the device realization

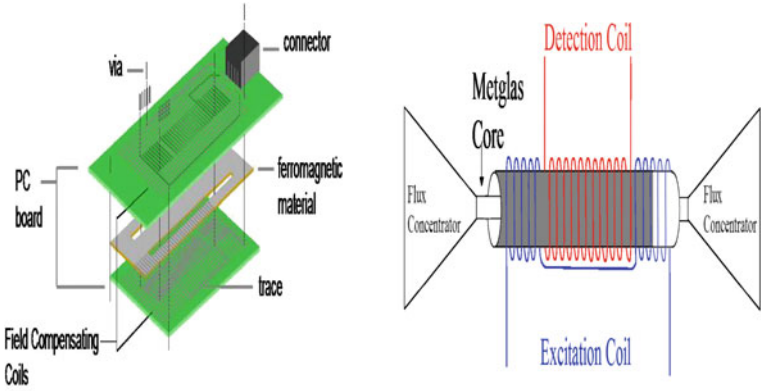

Fig. 2.40 Schematic of PCB fluxgate showing the core and windings *left* and the implementation of a "flux concentrator" *right*

Each wound-core (the "unit element" of the 3-core device) is constructed using a three-layer architecture. The two outer layers consist of standard printed circuit board (PCB) with copper wirings printed on them and the middle layer is the ferromagnetic material 2714 A by Metglas[1] in the un-annealed state (Fig. 2.40). There are two sets of printed wirings on each of the PCB's, corresponding to the driving (excitation) coil and the sensing coil. At the end of each wiring set are two small holes that are used for soldering to complete the winding circuitry when the components are put together. The middle layer is a sheet of the ferromagnetic material cut into a specific shape (Fig. 2.40), with outer dimensions 1.5×8.0 cm. The wound core is, then, realized by putting each ferromagnetic core in between the two PCB boards and aligning the holes at the ends of the printed copper wirings of the two boards. A small copper wire is passed through the holes from one board to the other and solder is used to fuse the wire in place. The two PCB boards are fused together in this manner to complete the windings for the sensing and excitation coils.

The ferromagnetic material comes from the manufacturer (METGLAS Inc.) in the un-annealed state, which means that the magnetic domains inside the material are oriented randomly. The sensor's response is greatly improved by annealing the ferromagnetic material after cutting it into shape to align all the domains in a particular direction, resulting in a cleaner and sharper signal. In the annealing process, a dc magnetic field is applied along the long axis of the material; in this setup, the sensor shows the greatest improvement in its response compared to the non-annealed case. Further improvement of the sensor can be achieved by employing more than one layer of the ferromagnetic core in each sensor. The multiple layers are electrically insulated from one another to prevent Eddy currents from passing from one core to the other. In the Metglas version of the sensor, we also incorporate a "flux concentrator" (made of Metglas), see Fig. 2.40. Unlike the micromechanical modulating flux concentrator

[1] See http://www.metglas.com for the magnetic characteristics of the material.

implemented by Edelstein [107] as a means to heterodyne detection away from the $1/f$ regime (see also [58] where a form of noise-mediated heterodyning has been discussed), our concentrator is static; it behaves like a large funnel concentrating more input magnetic flux along the long axis of the core. The static version implemented by us is also unencumbered by its own noise-floor, a constraint that can affect the operation of the modulating version.

The cores are mounted on the faces of a structure with a triangular section for orienting all of them in the same direction and then coupled through electronic circuits wherein the voltage readout (i.e., the time derivative signal of the flux detected by one of the sensing coils) is amplified by a voltage amplifier. Next, the signal is passed through an integrator to convert the derivative signal seen by the sensing coil back to the "flux" form so that the experimental system closely conforms to the model. Finally a Dead-Zone circuit trims out any dc in the output; specifically, it addresses (and removes) the dc drift that is endemic to the system. The signal then passes through an amplifier to achieve adequate gain to drive the adjacent fluxgate. Following this, the signal passes through a voltage-to-current converter (V-I converter) in its final step to drive the primary coil of the adjacent fluxgate. The setup is repeated for the other two coupling connections for the remaining cores and all values of the coupling circuit parameters are closely matched from one set to the other. Each stage of the coupling circuit also employs high speed and high precision operational amplifiers (op-amps) to minimize the time delay in order to conform closely to the model since a knowledge of the state variable x_i is available instantly in the model.

A stability analysis of the model equations with respect to a delay in the signal shows no significant divergence in the behavior, if the delay time is limited to 10% the oscillation period. This point is very significant in the implementation of the actual device because there will always be delays in the electronic circuits due to the component response times, and the coupling circuit board presented here has about 2–4% of the period in delay time (depending on the choice of op-amps, resistors and capacitors used) when operating at relatively high frequency (around 150 Hz). Most of the time, the laboratory device has been operated in the 37–100 Hz regime, so that the delay is even smaller.

Readout Algorithm. Once the magnetometer is configured, as described above and illustrated in Fig. 2.41, the outputs of the coupled cores are sent for processing in order to extract the information about the target field being detected. The readout algorithm is illustrated in Fig. 2.42. The signals from the 3-core system are taken from each of the integrator stages and passed through a summing circuit; alternatively, the signals can be recorded after the Dead-Zone stages. The output of the summing circuit is then passed through a Schmitt Trigger. If the signal is greater than the upper threshold value of the Schmitt Trigger, then the output is a HIGH corresponding to +10V. The output remains HIGH until the input signal falls below the lower threshold value of the Schmitt Trigger, which then outputs a LOW corresponding to −10V. In essence, the Schmitt Trigger converts the output into a clean dichotmous signal, retaining only the all-important information about the locations (along the time axis) of the switching events. The output from the Schmitt Trigger is passed through a

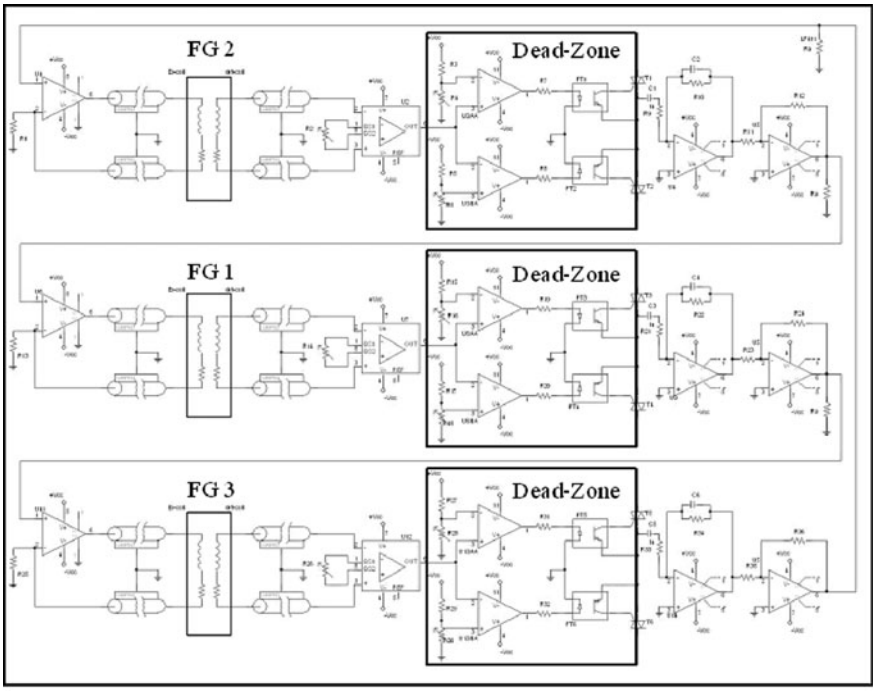

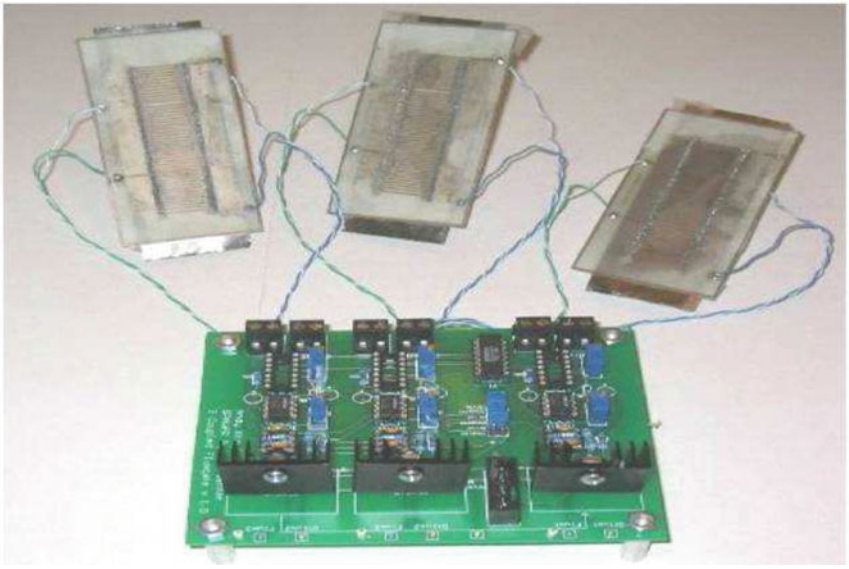

Fig. 2.41 *Top* Detailed circuit diagram as implemented in the laboratory. Using the Dead-Zone circuit helps solve the dc drift problem that is endemic to the system. Using this circuit to implement coupling, both the oscillation waveforms and the frequency scaling as a function of either the coupling strength or the applied dc field are in good (qualitative) agreement with the numerical results. *Bottom* Actual CCFM Device

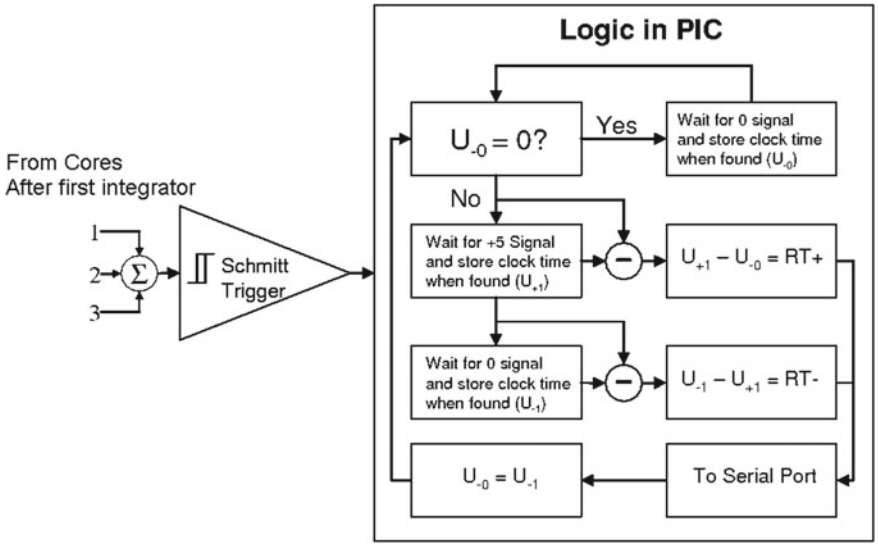

Fig. 2.42 Readout diagram and logic flowchart for the implementation of a coupled-core fluxgate magnetometer

voltage divider and diode to convert the signal to TTL in which +5V corresponds to a HIGH and 0 V corresponds to a LOW. This HIGH and LOW state is then passed to a programmable integrated circuit (PIC) microcontroller for further processing as seen in Fig. 2.42. When the system is started, it first looks for the LOW state. At the time this state is reached, the PIC is instructed to retrieve the clock time from the counter and mark that time as the previous lower threshold crossing time. Next, the PIC waits for a HIGH state. When reached, the PIC retrieves the clock time again and marks that time as the upper threshold crossing time. Then the PIC waits for the next LOW state, at which point it, again, retrieves the clock time and marks that time as the lower threshold crossing time. The procedure is repeated for the duration of the observation time. The residence time is determined as follows: the lower residence time (T_-) is the time difference between the crossing time of the upper threshold and the crossing time of the previous lower threshold; the upper residence time (T_+) is the time difference between the crossing (in the upward direction) time of the lower threshold and the next crossing (in the negative direction) of the upper threshold. Clearly the rapid time constant τ_F ensures that the crossing events are extremely rapid (compared to the residence time in each steady state); in the dichotomous time-series output of each fluxgate, this is characterizeded by sharp near-vertical transitions between the states. The presence of a moderate noise floor manifests itself in fluctuations in the steady states of each sensor, so that the successive residence times in any given steady state are not the same.

In practice, both the upper and lower residence times are accumulated for an appropriate number (10−15 in our laboratory setup, but adjustable, depending on the circumstances of the application) of oscillation cycles. A mean and a standard deviation are then computed for both. If the external signal is zero, then the mean values $\overline{T_{\pm}}$) are the same (within the first standard deviation). If the external signal is nonzero, then $\overline{T_{+}}$ is different from $\overline{T_{-}}$. The difference of the two values is proportional to the external field in the small ε limit, as already noted in Sect. 2.5. Since there is inherent noise within the system, the standard deviation is always nonzero for both residence times.

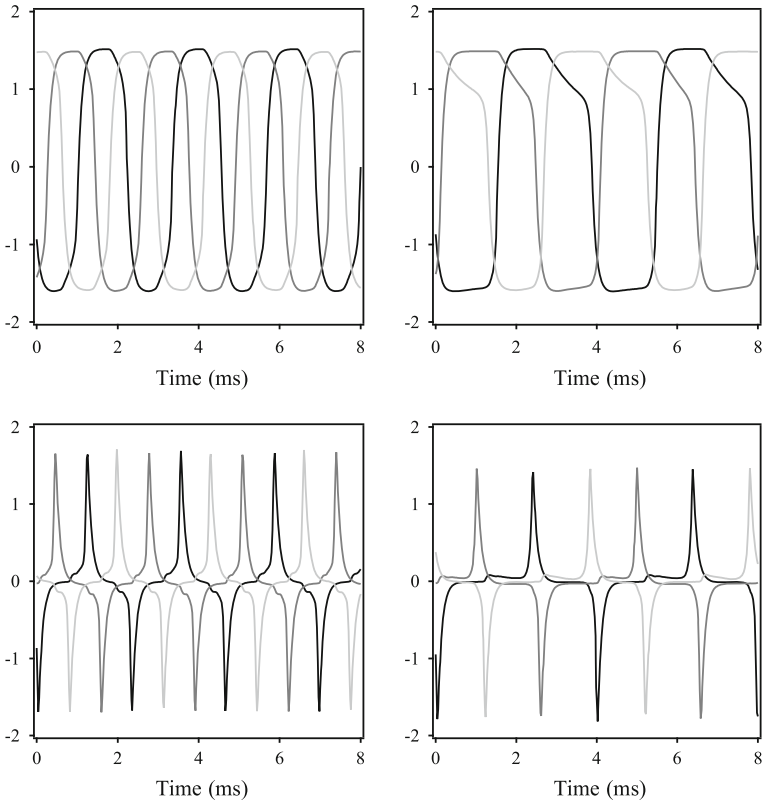

Fig. 2.43 Time series from the experimental system (standard configuration) for $\varepsilon = 0$ (*left column*) and $\varepsilon = 6.0\mu$ T (*right column*). The *top figures* show the traveling wave pattern illustrating the oscillation of the three coupled cores. Each one has the same amplitude and frequency but each is phase shifted by 120° as observed in the numerical model. The *bottom figure* shows the outputs (of the integrators) as seen by the sensing coils of the coupled device. The signals are recorded after the instrumentation amplifier stages in Fig. 2.41. The response matches, qualitatively, the theoretical results derived earlier [195]. $\lambda = -0.8$ in both cases

Experimental Results. The oscillations observed from our coupled setup are quite striking (Fig. 2.46). The system readily oscillates in a travelling wave pattern and, like the model, it favors this pattern no matter how many times it is restarted. As already noted, the "oscillations" correspond to (sequential) transitions over the energy barrier in the ring elements. The oscillation frequency in the experiment is about 57 Hz (this is, of course, adjustable via the parameter λ). Each wave is phase shifted by exactly $\frac{2\pi}{3}$ as predicted by the model. Comparison of the experimentally obtained oscillations to the numerical results (as shown in Figs. 2.14 and 2.43) shows good agreement with the caveat that, since the values of c and the time constant τ_F in the actual device (we set $\tau_F = 1$ in the model) are not known, we cannot correctly compare the time scales in the model and the experimental observations. The amplitudes of the oscillations in the experiment are also arbitrary in comparison to the model because the recorded voltages depend on the gains set in the coupling circuit. The magnetic flux in the model saturates between ± 1, but in the devices this quantity cannot be measured directly. Of course, it is clear that, the timeseries depicted in Fig. 2.46 was obtained via the standard coupling arrangement (2.6). Further illustration of good agreement between the numerical system and the prototype system is the frequency scaling (Fig. 2.44), as a function of the coupling strength and also as a function of the applied (dc) field. As expected, the frequency of the coupled system should rise as the square root of the coupling strength; further, as the applied field magnitude increases, the frequency decreases until the coupling strength is at the critical value where the oscillations cease to exist. Increasing the coupling values beyond this point will not

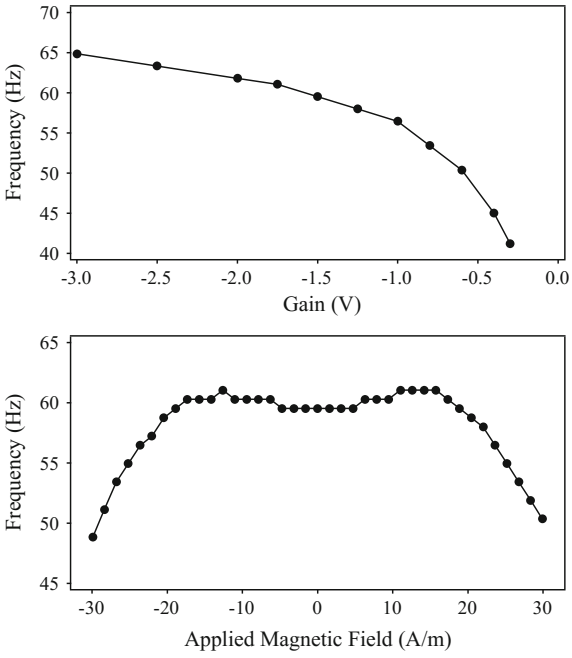

Fig. 2.44 Frequency scaling with respect to the coupling strength, expressed as a gain (*top*) and the applied dc target magnetic field (*bottom*)

produce any oscillation. We recall that, in the convention adopted in the theoretical description of this system, the coupling is *negative*, so that an"increase" of coupling implies that the coupling coefficient λ approaches zero. Similarly, increasing the applied field in either direction away from zero will reduce the frequency of the oscillations as predicted by the model; the oscillations cease to exist when the applied field is too large because the field moves the system past the critical point of the onset of the oscillation. The above behavior (already referenced in the preceding section) is evident from Eq. (2.18) which shows that the critical coupling parameter is ε-dependent. Accordingly, for a fixed coupling λ, the difference $\lambda_c - \lambda$ approaches zero with increasing ε, corresponding to an increased oscillation period. When this difference is zero (negative), the oscillations have infinite (imaginary) period and have ceased to exist.

Figure 2.45 shows a family of responsivity curves as a function of the applied field for different coupling strengths; the figure agrees well with the theoretically generated figure (not shown). The vertical scale is the ratio of the upper residence time over the lower residence time. The responsivity curves can also be created by taking the residence times difference; we choose to use the ratio because it is more responsive to small changes in the taret signal, as discussed earlier. The slopes of the curves indicate how responsive the coupled core system is to the applied field. As the coupling strength is increased toward the critical value, the responsivity curve becomes steeper. The greatest sensitivity is realized when the coupling strength is set closest to the critical value, but in this regime it can only detect a very small target field amplitude. Hence, the ability to tune the coupling to detect a range of target field strengths, must be a central feature of this mode of operation; when implemented, it

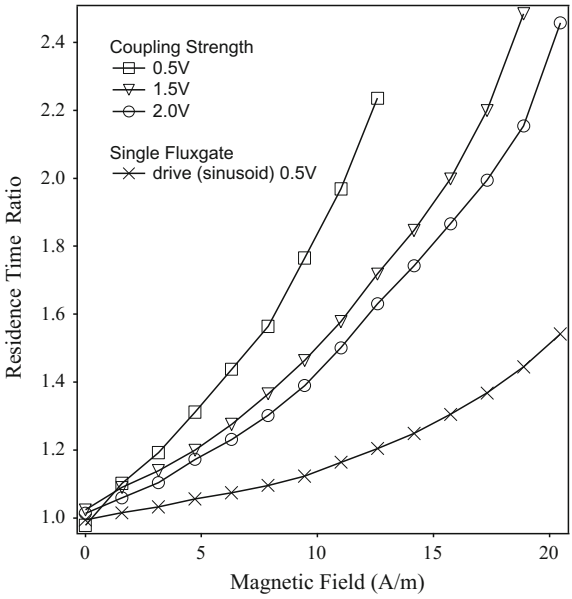

Fig. 2.45 Responsivity curves, using the Residence Time Ratio (RTR) versus the applied target magnetic field ε for different coupling strengths. As expected, the coupled core system is less responsive as the coupling strength is increased (top 3 curves). The *bottom curve* is the responsivity of an "equivalent" single core fluxgate magnetometer with bias signal amplitude selected to be slightly suprathreshold, thereby yielding the maximal sensitivity

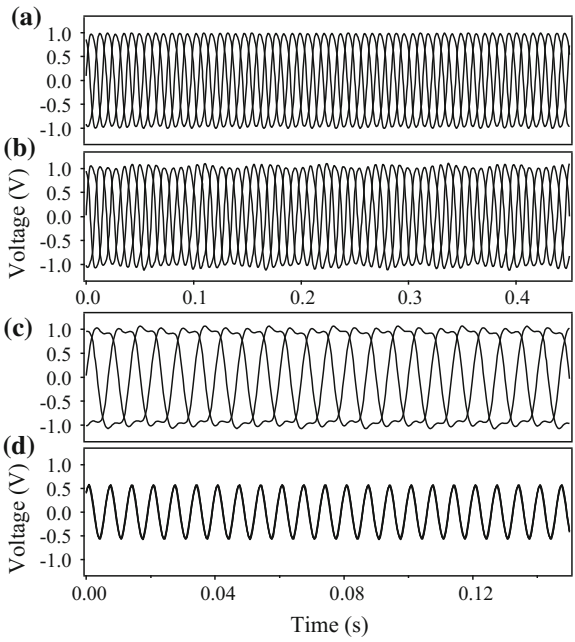

Fig. 2.46 Oscillation waveforms associated with the different regimes in the *experimental* system. **a** Oscillations (at 44 Hz) in the supercritical regime (see Fig. 2.25) without an external field. **b** Characteristic modulation of the oscillations in the supercritical regime with a small applied ac signal (at 150 Hz). **c** Oscillations in the subcritical regime where the system oscillates at $\omega/3$ (50 Hz) with no modulation of the waveforms. **d** Oscillations in phase to each other and frequency-locked to the external signal. The external signal amplitude increases from panels **(a)** to **(d)**

presents a capability where one may tune the coupling to reduce the sensitivity and increase the operating range, or vice versa.

Detection of AC Signals. We have validated our theoretical results on the detection of AC signals, see Sect. 2.7, via an experiment consisting of three coupled fluxgate magnetometers. The experimental setup is similar to the previously described case for dc target field detection [195], hence, details of the coupling circuitry and the construction of the fluxgates are not given here. The system's behaviors (Fig. 2.46) agree well with the theoretical predictions for detection of ac signals. In the experimental run, the system is setup with the coupling strength in the supercritical regime so that it is oscillating (44 Hz) without any applied external field (top panel of Fig. 2.46). The next panel illustrates the modulation of the oscillation waveforms by a small amplitude ac external signal (at 150 Hz) while the system is still in the supercritical regime; note that the the system remains oscillating at the natural frequency (44 Hz).

Thereafter, increasing the amplitude of the ac signal pushes the coupled system into the subcritical regime (see Fig. 2.25), and the resulting oscillations occur (panel (c) of Fig. 2.46) at $\frac{1}{3}$ the frequency of the ac signal without the amplitude modulation of panel (b). The last panel illustrates the case when the ac signal amplitude is increased sufficiently (into region III) so that the system switches to another behavior in the subcritical regime where all three waveforms are phase-locked to each other and the oscillation frequency exactly matches that of the external signal. All four scenarios illustrated here are predicted by theory, as is illustrated in Fig. 2.25 and verified in numerical simulations.

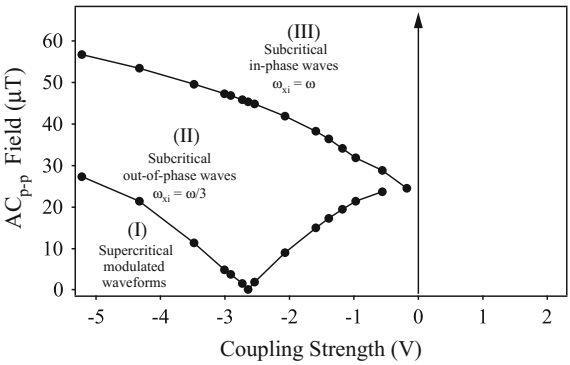

Fig. 2.47 Parameter space in the *experimental* system, confirming the different oscillation regions theoretically predicted in Fig. 2.25

Figure 2.47 provides experimental confirmation of the various oscillation regimes (of Fig. 2.25). The lines that separate the various regions are not quite as linear as those of Fig. 2.25 but it qualitatively confirms the existence of the oscillation regimes. The slight inconsistencies arise, possibly, from the device differences because the ferromagnetic cores were non-identical, and their magnetic domains were oriented differently. In addition, the coupling circuit components were nonidentical so that the coefficient λ was not the same for all the components of (2.6). Finally, there was a small dc voltage in the coupling circuitry that acted like an external dc signal which we could not completely remove.

The work in [195] demonstrates that unidirectional coupling and a judicious choice of initial conditions (that are, actually, the most natural for any experimental setup) can lead to oscillatory behavior (with a characteristic square root scaling of the response period) in overdamped bistable systems even in the absence of an external forcing signal; in the presence of an additional dc target signal, the oscillation characteristics change, in turn this can be exploited to characterize the target signal. This letter considers the first known treatment of emergent frequency dependent phenomena when the coupled system is subject to a time-periodic external forcing. While a detailed analysis of each regime in Fig. 2.25 must be deferred to an upcoming paper, we note here the richness of behavior in different regimes of the parameter space of coupling and forcing signal amplitude; it is particularly noteworthy that the theoretical phase diagram has been validated experimentally and the experimental time series response in the different regimes agrees (qualitatively) with the results (not shown) of numerical simulations. The emergent behavior can be used to quantify time-periodic target signals (since the internal oscillation frequency, (44 Hz in our setup) can usually be controlled by an appropriate choice of system parameters. The results of this work are expected to be applicable to a large class of nonlinear dynamic systems coupled in this manner.

Sensor performance. It is appropriate to discuss the effect of the sensor noise floor on the response; in a real application, this noise can arise from internal (materials, electronics, etc.) sources, as well as contamination of the target signal. The voltage output signal from a single core fluxgate (operated via the residence times readout)

has been shown [10, 11] to have a noise component that can be well-approximated by a gaussian distribution. However, the individual residence times have noise components which are, in general, non-gaussian; they have noise-dependent tails and, with increasing noise intensity the tails get longer, a feature that is quite common to two-state devices. Our earlier theoretical and experimental work [60] showed these features, and also showed that decreasing the noise intensity (alternatively, increasing the bias amplitude A) reduced the tail and made the distributions more gaussian-like; in the small σ^2/A limit (where σ^2 is a theoretical noise variance) the residence times distributions are gaussian [60], which also has been observed in the experiments. Of course, this comes at the price of reduced sensitivity (since the sensitivity, for the residence times readout, is inversely proportional to the bias amplitude). The above ratio can be reduced (for a given noise floor) by increasing the bias amplitude A, but this increases the onboard power reqauirement as well as the contribution to the noise floor arising from the reference signal generator. A careful optimization of geometrical and other core parameters is also known to lower the noise in the voltage signal (see e.g. [224]).

To better understand the ramifications of background noise, we have introduced [60] the (critical to a practical system) observation time T_{ob}, and defined a response signal-to-noise ratio (SNR) which is directly proportional to $\sqrt{T_{ob}}$. A longer observation time leads to an enhanced response (to very weak target signals), however, practical constraints may limit T_{ob}. One can increase the bias frequency ω, thereby increasing the number of crossing events and improving the statistics of the measurement process, however this implies a larger power requirement. Hence, in a practical application, one must strike a balance between the physical constraints (e.g. onboard power, noise from the bias signal generator) and the need to carry out a reliable measurement of the mean RTD. The practical configuration is also, of course, heavily dependent on the amplitude (relative to the energy barrier height) of the target signal ε to be quantified; it helps to have an *a priori* idea of the range of target signals under consideration for a given application. However, if the target signal is larger than the energy barrier height (or, roughly, the coercive field) it is, usually, easier to detect it by standard techniques that do not require a finely adjusted sensor such as the one described in this work.

The noise floor of the (single core) residence times fluxgate can be obtained via the power spectral density of a time series of the voltage response, taken at $1\,Hz$ (usually); this provides a good basis for comparison to existing fluxgates that utilize a spectral readout [45, 337]. In the RTD readout the effects of noise are, usually, manifest in uncertainties in the crossing times at the lower and upper thresholds. The ensuing uncertainty (in the time-domain) has been, formally, connected [11] to an uncertainty in the amplitude domain i.e., to an equivalent noise-floor [337] that one would obtain via an output power spectral density.

A Performance Measure: The Resolution. The RTD readout that we use in our devices is very simple to implement; one requires a clock and a counting circuit to keep track of the crossing events of the upper and lower thresholds, and a running arithmetic mean of the residence times in the up and down states. The quantity

of interest is, then, the mean RTD, denoted by $\overline{RTD}$. As already pointed out, the conditions for achieving optimal performance via this readout scheme, are in line with the conditions for having lesser onboard power and, hence, a lower noise floor arising from the power supply and readout electronics. For the CCFM, the bias signal generator that is necessary for the single core device is absent and, with it, a significant source of noise; however, one still has to contend with a noise floor arising from the readout and coupling electronics, external noise (contaminating the target signal), and the magnetic noise in the cores. In our most recent implementations of the sensor, we use ultra low noise electronics and implement the RTD readout in CMOS, in order to further lower the noise floor. In addition, the magnetic noise in the cores is significantly reduced by using a core of (approximately) single domain thickness.

We now introduce the "Resolution"; it is the minimum magnetic field that can be discriminated by the sensor against the background. In this context, it is very important to note that our sensors have been designed to null out stationary ambient magnetic fields arising from terrestrial magnetism, parked vehicles, etc. The nulling process takes around 20s from cue and, once complete, allows the sensor to discriminate magnetic fields (from slowly moving ferrous objects having a *static* magnetic signature) that are well below the ambient (static) magnetic field. We also emphasize that the CCFM is well-suited to the detection and analysis of time-periodic magnetic signatures [194], however, we have focused on the dc target signal case, throughout this book. The Resolution is defined as:

$$R = \frac{STD}{\frac{\partial \overline{\Delta_1 t}}{\partial \varepsilon}} \tag{2.73}$$

where $\overline{\Delta_1 t}$ represents the averaged RTD and the denominator is simply the slope of the output-input transfer characteristic (the plot of $\overline{\Delta_1 t}$ versus the target signal ε), and represents the device responsivity. For small target signals, we expect this slope to be independent of ε (i.e. $\overline{\Delta_1 t} \propto \varepsilon$); this is, of course, convenient for practical applications. The numerator in (2.73) is the standard deviation of the RTD, i.e., $STD(\Delta_1 t)$.

We now describe how this quantity is measured, experimentally, in a CCFM consisting of $N = 3$ cores following the AO dynamics (2.26), i.e., the "favored" element for measuring the RTD is $x_1(t)$. We use an observation time (once the ambient static magnetic field nulling has been achieved) of 0.1 s and an oscillation frequency that is adjusted (via the coupling λ) to yield 15–20 cycles of the response during this observation window. Of course, the observation time can be increased, but this would depend on the circumstances of the particular application and, more importantly, on the statistics and stationarity (or lack thereof) of the ambient noise. Keeping ε fixed, we compute a time-averaged RTD $\Delta_1 t$ (via the x_1 element) by averaging the RTDs obtained in the observation window. The experiment is then repeated several times for the same ε; each repetition yields a time averaged (over the observation window) RTD which is not necessarily the same as the others, due to fluctuations. In this way,

one obtains a large number of time averaged RTDs corresponding to the fixed value of ε. The process is repeated for different values of ε. The quantity $\overline{\Delta_1 t}$ is, then, the statistical average of these points (for the same value of ε). A plot of $\Delta_1 t$ versus ε shows clusters of discrete points (each point corresponding to an average over the observation window) for each value of ε. The locus of the statistical means of each cluster of points then yields a straight line (for very small ε) whose slope yields the responsivity, i.e., the denominator of (2.73). In Fig. 2.48, we have plotted the "return map" of the (experimentally obtained) RTDs. For a given ε, each data point in a cluster represents the (window-averaged) RTD at 2 successive observation intervals each 0.1 s long; thus, we generate a cluster of points corresponding to a plot of $RTD(t_{n+1})$ versus $RTD(t_n)$. Each cluster of points corresponds to one value of the target field ε; in this experimental sequence (Fig. 2.48), the point clusters correspond to values of ε that are approximately $9.89\,nT$ apart. The density function of each cluster is near-gaussian, with a mean value corresponding to the averaged RTD over all the discrete points, and a standard deviation that can be computed from the observations. The locus of the mean values is the straight line. When one plots these mean RTD values as a function of ε (not shown), the slope of this line (the responsivity, i.e. the denominator of (2.73)) is $165.08\,sT^{-1}$. In the figure, the standard deviations of the point clusters are (from left to right) 5.53×10^{-8}, 5.35×10^{-8}, 4.91×10^{-8}, and 4.99×10^{-8}, resulting in resolutions (calculated from (2.73)) of 335, 324.15, 297.58, and 302 pT respectively. The resolution is approximately constant (the deviations arise from experimental uncertainties and fluctuations) in this regime of low target signal. In this context, it is worth noting the obvious: in a totally noise-free environment, the clusters of Fig. 2.48 would be replaced by single points woth the gaussian distribution of the points (in each cluster) collapsing to a delta-function in the zero noise limit. It is important to realize that, as ε increases, the target signal becomes more easily "resolved". However, the analytic description of the response breaks down when ε becomes comparable to (or exceeds) the energy barrier height of a single element (isolated) potential; in this regime, the resolution becomes ε-dependent (see below).

One expects, at least in the linear regime (ε very small), that the distribution of the discrete points corresponding to a given ε will be near-gaussian; this is, in fact, observed in our experiments. The numerator in (2.73) is also computed, directly from the data, for each value of ε. The definition (2.73) should be compared with our heuristic definition of a response SNR [60]; we find, in fact, that the resolution is proportional to the inverse of the SNR. This is reasonable because a lower value of the resolution implies better performance, as does a higher value of the SNR. What is important to note is that the quantity in (2.73) incorporates the effects of the noise on the sensor performance in a simple manner that can be easily implemented in practice; we can use this quantity to make comparisons between different sensor versions.

In an experiment, one really cannot pin down the exact sources of background noise, and the statistics of the fluctuations are even more difficult to quantify. In SCFM experiments we found that the fluctuations in the RTD were approximately gaussian [11] in conformance with a theoretical model that was presented in [60]. For the CCFM, a careful analysis of the experimental results affords us the opportunity

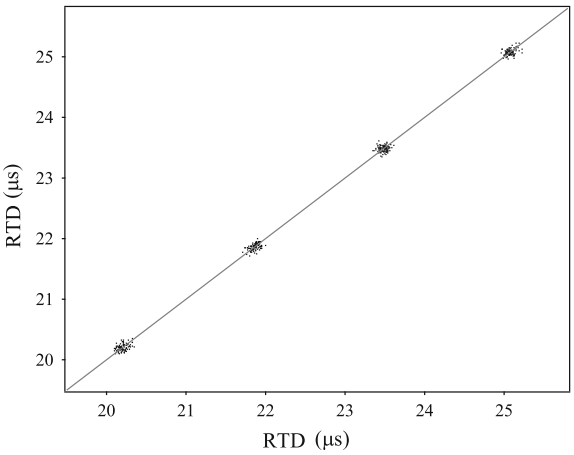

Fig. 2.48 Return map of the (experimentally obtained) RTDs; each cluster corresponds to a different ε and the straight line is the locus of the means. Each individual point in a cluster corresponds to an average of 15–20 values of the RTD taken in an observation time window (0.1s in this case). Standard deviation of each cluster is a function of ε (see text), while mean value is proportional to ε so that the responsivity (denominator of (2.73)) is an ε-independent number (see text). At low signal values, the resolution is, approximately, constant (see text). Parameters are: $N = 3$ cores and $\lambda = -0.8$

to develop simple theoretical models that (hopefully) will help us understand, at least qualitatively, the noise-mediated sensor dynamics.

To this end, we return to the definition (2.73) and its experimental computation, as described in the preceding subsection. We will try to obtain a theoretical expression for the resolution which, while not directly comparable to the experimentally obtained number, can at least afford an insight into the role of background noise. We focus on the scatter plot of Fig. 2.48 and assume that the individual points (corresponding to the averaging of several RTDs in an observation window) can be modeled as the response to an external dc magnetic flux that is gaussian distributed but does not change rapidly (specifically, it changes on time scales that are on the order of the observation window, typically 0.1 s). In other words, we assume that each of the window-averaged data points in this figure is uncorrelated with its predecessor, and arises from a different realization of the external signal, these realizations being drawn from a gaussian distribution with mean ε_0 and variance σ^2:

$$P(\varepsilon) = \frac{1}{\sqrt{2\pi\sigma^2}}\, e^{-(\varepsilon-\varepsilon_0)^2/2\pi\sigma^2}. \tag{2.74}$$

Then, the idea is to compute the statistics of the individual terms in the expression (3.15), with the appropriate factors of N so that we make contact with the AO configuration that is implemented in our laboratory devices.

We start by noting that we may write (3.15) in the form $\Delta_1 t = t_1 - t_2$ where we define,

$$t_{1,2} = \frac{N\pi}{\sqrt{cx_{inf}}} \frac{1}{\sqrt{(\lambda_{c0} - \lambda)x_{10} \pm \varepsilon}}, \tag{2.75}$$

with the negative sign of ε corresponding to t_1, λ_{c0} the critical coupling absent the target signal i.e., $\lambda_c = \lambda_{c0} - \varepsilon$ as readily observable in (2.18), and x_{10} represents the stationary position (potential minimum) of the solution at rest while the element that it is coupled to evolves (see, e.g. [195, 307]). Then, treating t_1 and t_2 as random variables and carrying out the appropriate change of variables [313] we obtain, after some calculation, the probability function:

$$P(t_1) = \frac{2\pi^2}{\sqrt{2\pi\sigma^2} c x_{inf} t_1^3} \exp\left[-\alpha(t_1^{-2} - t_{1d}^{-2})^2\right], \tag{2.76}$$

with a similar expression for the probability $P(t_2)$. Here, $t_{1d} \equiv \frac{\pi}{\sqrt{cx_{inf}}}(\delta_0 - \varepsilon_0)^{-1/2}$ and $t_{2d} \equiv \frac{\pi}{\sqrt{cx_{inf}}}(\delta_0 + \varepsilon_0)^{-1/2}$ are the deterministic crossing times, with $\delta_0 \equiv (\lambda_{c0} - \lambda)x_{10}$ expressing the distance of the dynamics from the critical point. We have also defined the constant $\alpha \equiv \pi^4/(2\sigma^2 c^2 x_{inf}^2)$.

Using the expression (2.76) we must find the mean values $\overline{t_{1,2}}$ and $\overline{t_{1,2}^2}$, *en route* to a computation of the terms in (2.73). We can, most easily, compute these averages via a Laplace expansion of the relevant integrals (the same procedure is adopted to normalize the probability) with the results:

$$\overline{t_{1,2}} = \frac{16\alpha + 3t_{1,2d}^4}{16\alpha} t_{1,2d}, \qquad \overline{t_{1,2d}^2} = \frac{2\alpha + t_{1,2d}^4}{2\alpha} t_{1,2d}^2. \tag{2.77}$$

We then obtain (recall that we are working with the AO configuration):

$$\frac{\overline{\Delta_1 t}}{N} = t_{1d} - t_{2d} + \frac{3}{16\alpha}(t_{1d}^5 - t_{2d}^5). \tag{2.78}$$

Since we are in the small (compared to the distance δ_0) ε regime, we can reduce the above expression to:

$$\overline{\Delta_1 t} = \frac{N\pi}{\sqrt{cx_{inf}}\delta_0^{3/2}}\left[1 + \frac{15}{8}\frac{\sigma^2}{\delta_0^2}\right]\varepsilon_0, \tag{2.79}$$

to leading order in ε_0. Note that, in this regime, the response transfer characteristic (in this case, the $\overline{\Delta_1 t}$ versus ε_0 curve) has a constant slope. We also find

$$\sigma_{t_1}^2 = \overline{t_1^2} - \overline{t_1}^2 = \frac{t_{1d}^6}{2\alpha}, \tag{2.80}$$

to $O(\sigma^2)$, with a similar expression for $\sigma_{t_2}^2$. The standard deviation of the RTD is then given, to leading order in ε_0, by

$$STD(RTD) \equiv \sqrt{\sigma_{t_1}^2 + \sigma_{t_2}^2} = \sqrt{\frac{\pi^2\sigma^2}{2cx_{inf}\delta_0^3}}\left[1 + \frac{3\varepsilon_0^2}{\delta_0^2}\right], \tag{2.81}$$

which, finally, leads to the relatively simple expression for the resolution:

$$R = \sqrt{\frac{\sigma^2}{2N^2}}\left[\frac{1 + \frac{3\varepsilon_0^2}{\delta_0^2}}{1 + \frac{15}{8}\frac{\sigma^2}{\delta_0^2}}\right]. \tag{2.82}$$

We note that, in the limit of very small noise variance, a Gram Charlier expansion (not shown) shows that the distributions $P(t_{1,2})$ approach gaussians. For arbitrary noise, however, the distributions have tails and their modes do not coincide with the deterministic mean values $t_{1,2d}$. In this context, we note that the first term in (2.79) is precisely the deterministic RTD in the small signal limit. For very small signals $\varepsilon_0 \ll \delta_0$ the resolution is independent of the target signal. This is, from the standpoint of detection, the most important regime. Large signals are easily detected without much need for sensor optimization or adjustment. In the (more difficult, practically) small target signal regime, however, one can optimize the sensor to yield the best achievable resolution and, more importantly, the resolution in this operating regime is a performance measure that is *independent* of the target signal. The results above could also be obtained by first constructing the density function of the RTD via the convolution, and then directly obtainng the first and second moments; the above procedure is, however, far less tedious.

We conclude this subsection by reiterating that the resolution R should provide a (at least) qualitative idea of what to expect in a real device; since quantities like the variance σ^2 of the external signal fluctuations are unknown (and cannot be isolated, in an experiment, from other noise sources), it is not feasible to compare (2.82) directly with the experimental results. The expression does show, however, that the resolution could be enhanced by increasing the number N of coupled cores; of course, the gain in resolution has to be balanced against the engineering complexity involved in constructing a magnetometer with $N > 3$ cores.

We currently have a SCFM that uses a single domain core material and PCB electronics; it has the dimensions of a mobile phone and draws about 150 mW of power. The resolution of this sensor is, approximately 500 pT. The sensor has been operated in an unshielded environment and utilizes the ambient field nulling mechanism described in the preceding section. It is anticipated that the entire RTD readout circuitry will be realized in CMOS in the very near future, thereby affording a far smaller package with lower power consumption and a lower sensor noise floor. At the same time, we have a laboratory version of the CCFM with the AO configuration. This sensor uses the same core materials and yields dynamic behavior that faithfully follows all the theoretical predictions. The resolution of this sensor is 200 pT; this is somewhat better than the sensor that was used in the experiments leading to the data

of Fig. 2.48. In principle, the resolution can be improved (i.e. the numerical value decreases) by incorporating a larger (odd) number of cores in our unidirectional coupling arrangement; this is readily apparent when we realize that the denominator of (2.73) scales, linearly, as N (this is also seen in (2.82)). However, increasing the number of cores comes at the cost of increased engineering complexity, and additional onboard power (for the coupling circuitry). In addition, the effects of increasing N on the magnetic noise floor are still under investigation, although the results shown in Fig. 2.28 provide grounds for optimism that increasing N will not degrade the response as long as we operate within well-defined regimes of optimal response (e.g. near the onset of oscillations as suggested in Fig. 2.28).

We also point out that, in recent laboratory realizations of the CCFM, parameter mismatch issues have been reduced to a minimum. The cores are near-identical (cut from the same sample of single-domain magnetic wire), and the coupling circuitry can also be set up so that the coupling coefficients λ are the same throughout the arrangement. Hence, while there are likely to be lingering mismathes in parameter values, they can be substantially minimized. Of greater concern, then, are the sources of noise arising from the readout electronics, the magnetic noise in the cores themselves, and fluctuations that are superimposed on the target signal. The effects of fluctuations arising from these sources have been addressed, to some extent, in this book and in our earlier work [59, 257]. This leaves another potential source of noise that can easily arise in practice, temperature fluctuations that affect the nonlinearity parameter c, particularly when the same device is operated in greatly different environments. The parameter c is proportional to the ratio T_c/T, T_c being the Curie temperature. Temperature fluctuations will, therefore, introduce a state dependent noise term in the coupled dynamics. In turn, the parameters λ_c as well as the positions of the fixed points of the core potential functions (for zero coupling) will also fluctuate. A systematic treatment of the effects of these fluctuations is beyond the scope of this book, and will be the subject of future work.

It is worth reiterating that the idea of threshold crossing events leading to a quantification of external signals is deeply rooted in the computational neuroscience repertoire wherein one analyses the response of a single neuron, or even a small network, to a stimulus by examining the statistics of the point process generated by successive threshold crossings or "firings". Hence, our readout scheme actually leads to an implementation of these sensors as "neural"-like devices

Finally, it should be clear that our coupling scheme is quite readily applicable to a vast array of dynamical systems which follow the basic "particle-in-potential" paradigm with U being any bi- or multi-stable potential and x the appropriate state variable. The ability to control the oscillation frequency (the laboratory realization of the CCFM can be made to oscillate at frequencies ranging from a few Hz to several kHz, for example) dramatically broadens the range of applications that can benefit from this scheme. We note that the response of the CCFM to time-sinusoidal magnetic fields has been described (and quantified in the laboratory) [194]. Hence, although we have focused on the case of a dc target signal in this review, we emphasize that there is a richness of nonlinear dynamic behavior that can be exploited in the detection of time-periodic magnetic fields.

http://www.springer.com/978-3-662-55543-9

Symmetry in Complex Network Systems
Connecting Equivariant Bifurcation Theory with Engineering Applications
In, V.; Palacios, A.
2018, XV, 406 p. 259 illus., 112 illus. in color.,
Hardcover
ISBN: 978-3-662-55543-9